Multisourced CO₂ Injection in Fan Delta Conglomerates and Its Influence on Reservoir Quality: Evidence from Carbonate Cements of the Baikouquan Formation of Mahu Sag, Junggar Basin, Northwestern China

Ning Zhu [1], **Yingchang Cao** *[1], **Kelai Xi**[1], **Songtao Wu**[2,3,4], **Rukai Zhu**[2,3,4], **Miaomiao Yan**[1], **Shunkang Ning**[5]

1. *School of Geosciences, China University of Petroleum, Qingdao 266580, China*
2. *Research Institute of Petroleum Exploration and Development, CNPC, Beijing 100083, China*
3. *Key Laboratory of Oil and Gas Reservoirs, CNPC, Beijing 100083, China*
4. *National Energy Tight Oil and Gas R&D Center, Beijing 100083, China*
5. *Wenliu Oil Recovery Plant of Zhongyuan Oilfield Branch, Puyang 457000, China*

Ning Zhu: https://orcid.org/0000-0001-8500-6206; Yingchang Cao: https://orcid.org/0000-0002-1606-5752

ABSTRACT: Sandy-conglomerate reservoir has gradually become a major target of oil and gas exploration. Complex diagenetic process and diagenetic fluid play a significant role in affecting reservoir heterogeneity. Carbonate cements form at various stages of the diagenesis process and record various geological fluid information. Recently, one-billion-ton sandy conglomerate oil field was exposed in Triassic Baikouquan Formation, Mahu sag, Junggar Basin. Therefore, an integrated study applying casting thin sections, cathodeluminescence, fluorescence, carbon and oxygen stable isotopes, electronic probe microanalysis and aqueous fluid inclusions measurements was performed in order to identify the types of carbonate mineral and its representative diagenetic environment and discuss the influences of different CO₂ injections on reservoir quality. The main findings are as follows: The reservoir is mainly composed of 70.33% conglomerate and 16.06% coarse-grained sandstone. They are characterized by low compositional maturity and abundant lithic debris. Four types carbonate cements are identified according to the petrological and geochemical characteristics, including two types of Mn-rich calcite, ferran calcite, siderite and dawsonite. They display an unusual broad spectrum of δ¹³C values (-54.99‰ to +8.8‰), suggesting both organic and inorganic CO₂ injections. The δ¹³C values of siderite are close to 0, and its formation is related to meteoric water. The δ¹³C values of ferran calcite and the occurrence of dawsonite indicate the trace of inorganic mantle-derived magmatic fluids. The δ¹³C values and trace elements of Mn-rich calcite record the information of hydrocarbon-bearing fluids. The fluid inclusions measurement data and reservoir properties and oil-test data show that the oil content of reservoir is not only affected by the formation time of different cements, but also by the relative content of dissolution and cementation. For these reservoirs altered by carbonate cements, it does not cause poor oil-bearing due to blockage of secondary minerals.
KEY WORDS: carbonate cement, CO₂ fluid, carbon and oxygen isotope, reservoir, Mahu sag, Junggar Basin.

0 INTRODUCTION

As a member of subtle reservoirs, sandy conglomerate reservoirs are widely distributed despite their small proportion (Liu et al., 2012; Yuan et al., 2002). For example, the Tertiary conglomerate in the Veracruz Basin, Mexico (Helu et al., 1977), the Alberta and Columbia Cretaceous conglomerate (Nodwell and Hart, 2006), the Pennsylvania basement conglomerate in Kansas (Rogers, 2007), the Hemlock Group conglomerate in the Alaska field (O'Sullivan et al., 1991), the Norwegian North Sea Triassic conglomerate (Mahmic et al., 2018), and the Pliocene conglomerate in the Los Angeles Basin (Edwards, 1934), Morrow chert conglomerate in the Anadarko Basin, Oklahoma (Shelby et al., 1980). In China, from the 1970s to the 1980s, the exploration of conglomerate reservoirs in the Bohai Bay Basin has made breakthroughs once and again, and its exploration results have important guiding significance for conglomerate reservoirs in other places (Yuan et al., 2002). In recent years, sandy conglomerate reservoirs with proved reserve of more than 1 billion tons have been discovered in the western slope of the Mahu sag, Junggar Basin, becoming the largest conglomerate field in the world (Hao et al., 2018). However, extremely strong heterogeneity of these sandy conglomerate reservoirs mainly caused by diagenesis, seriously affects exploration

---

(Arnott, 2003; Cant and Ethier, 1984).

The authigenic mineral can well record the whole process of diagenesis and the transformation of the diagenetic environment (Worden, 2006; Moore et al., 2005). Generally, the authigenic zeolite reflects the activity of fluid rich in Ca, Na elements in alkaline environment (Wang et al., 2018). The authigenic quartz reports the signs of Si-rich fluid in acid environment, while the authigenic clay minerals reveal their precipitation of partial ions in a closed diagenetic environment after the dissolution of mineral particles (Wang et al., 2018; Zhu et al., 2012). Besides, carbonate minerals usually reflect the fixation of CO_2 from some kind of source in subalkaline environment. These carbonate minerals formed from different sourced CO_2 are diverse and exist in various stages of sedimentary and diagenesis. They are characterized by various lithological features, dissolution and recrystallization ability, which have important influence on reservoir physical properties (Duan et al., 2017; Wang et al., 2015). In addition, they can record information about material transfer process and CO_2 fluid types, reflected in lithofacies and geochemistry (Stroker et al., 2013; Wang et al., 2007).

Therefore, the study of carbonate minerals associated with these fluids is of great importance to the discussion of geological events that can affect the heterogeneity of oil and gas reservoirs. Carbonate cements act as a recorder of geological fluids, and they have been extensively and exhaustively researched on the characteristics of mineralogy, texture and chemical compositions (Chowdhury and Noble, 1996), the formation mechanism (Hu et al., 2018; Yang et al., 2018; Wang et al., 2016; Xi et al., 2016; Milliken et al., 1998), and the influence on reservoir heterogeneity (Javanbakht et al., 2018; Kang et al., 2018; Cui et al., 2017; Fontana et al., 2014; Morad et al., 2010; Dutton, 2008; Chi et al., 2003; Rossi et al., 2001). Most of the previous research on carbonate minerals is mainly related to the organic CO_2 fluid formed by acid decarboxylation and there is no comparative study on multi-material sources and multigenetic carbonate cements. Therefore, conducting refined studies on carbonate cements is of great importance for evaluating and predicting geologically appropriate reservoirs.

For the sandy conglomerate reservoir of the Triassic Baikouquan Formation (T_1b) in the western slope of the Mahu sag, Junggar Basin, the basic characteristics of diagenesis were studied and the phenomenon of feldspar dissolution was also reported (Kang et al., 2018; Xiao et al., 2018; Jin et al., 2017), indicating the alteration of reservoir by diagenetic fluid. The systematic research on complex diagenetic fluids is still weak. We observed that many types of carbonate cements were developed in the research area, and their petrological and geochemical characteristics showed great differences, which indicate the occurrence of multiple CO_2 injections and complex diagenetic fluids. Therefore, taking the sandy conglomerate of T_1b in the west slope of Mahu sag, Junggar Basin as an example, a series of optical analysis and geochemical analysis were used to determine the mineral types and typical diagenetic environment of carbonate rocks and discuss the influences of different CO_2 injections on reservoir quality. This investigation not only provides important guidance for hydrocarbon exploration, but also provides a good example for the study of cement heterogeneity of gravel reservoirs filled with differential fluids.

1 GEOLOGICAL SETTING

The Junggar Basin is an important transpressional superimposed basin in western China, developed from Early Paleozoic to Quaternary and deposited from Carboniferous to Quaternary (Li et al., 2012; Zou et al., 2005). It could be further subdivided into 5 first class tectonic zones and 32 secondary class tectonic zones, and different structural units have experienced quite different evolution histories, fluid flow environments, fluid conduit frameworks and petroleum accumulation histories (Zou et al., 2005) (Fig. 1a).

The study area, Mahu sag slope area, is located in the foreland thrust belt of northwest margin of the Junggar Basin and belongs to the Central depression zone. Its tectonic evolution is controlled by the two boundary fault zones, the Wuxia fault zone and Kebai fault zone (Chen et al., 2015). The evolution of Junggar Basin consists of the following five phases: (1) postorogenic stretch in Early Permian, (2) strong extrusion thrust in Middle–Late Permian, (3) inherited thrust superposition in Triassic, (4) overall oscillating rise and fall in Jurassic–Cretaceous, and (5) the intra-continental foreland in Cenozoic. Altogether, the tectonic activity in this area was intensive before Triassic and tended to be stable after Triassic (Lei et al., 2005). There are three groups of fracture patterns developed in the Mahu sag slope area: (1) Type I faults are compression-torsional faults that are near parallel to the boundary faults from the Middle Hercynian to Indosinian Stage; (2) Type II faults are strike-slip faults that are perpendicular to the boundary faults, and the formation time was from the Middle Hercynian to Himalayan Stage; and (3) Type III faults are sheared by Type I and II faults, which are mostly interlayer faults and were formed from the Middle Indosinian to Yanshanian Stage. Although the specific channel characteristics of different stages are different, and the active intensity of strike-slip faults is weakening, most of them cut through the Triassic strata, even the Jurassic and Cretaceous strata (Chen et al., 2015; Tan et al., 2008) (Fig. 1b). These complicated faults cannot be the only dominant migration pathway of oil and gas as the diagenetic fluid can also enter the reservoir along these faults, which has a major effect on the diagenesis of the reservoir. Sediments filling the basin comprise Carboniferous (C), the Lower Permian Jiamuhe (P_1j), Fengcheng (P_1f) Formation, the Upper Permian Xiazijie (P_2x), Wuerhe (P_2w) Formation, the Lower Triassic Baikouquan (T_1b), the Middle Triassic Kalamay (T_2k), the Upper Triassic Baijiantan (T_3b) Formation, the Jurassic Badaowan (J_1b), Sangonghe (J_1s), Xishanyao (J_1x), Toutunhe (J_2t), Guqi (J_3q) Formation and Cretaceous strata (Cao et al., 2006) (Fig. 2). There are seven sets of reservoir-caprock combinations, and the P_1j and P_1f are the main source rocks (Cao et al., 2006). The T_1b, one of the main reservoirs, is composed of coarse clastic sedimentary rocks (mainly conglomerate) that were deposited in alluvial fans near the western piedmont (Kang et al., 2018). Previous studies have shown that there is no obvious uplift and denudation in the T_1b strata.

2 SAMPLES AND METHODS

The study was based on 214 sandy conglomerate samples from 21 core wells in T_1b at a burial depth from 2 416 to 3 925 m. The additional rock composition data of 255 thin section
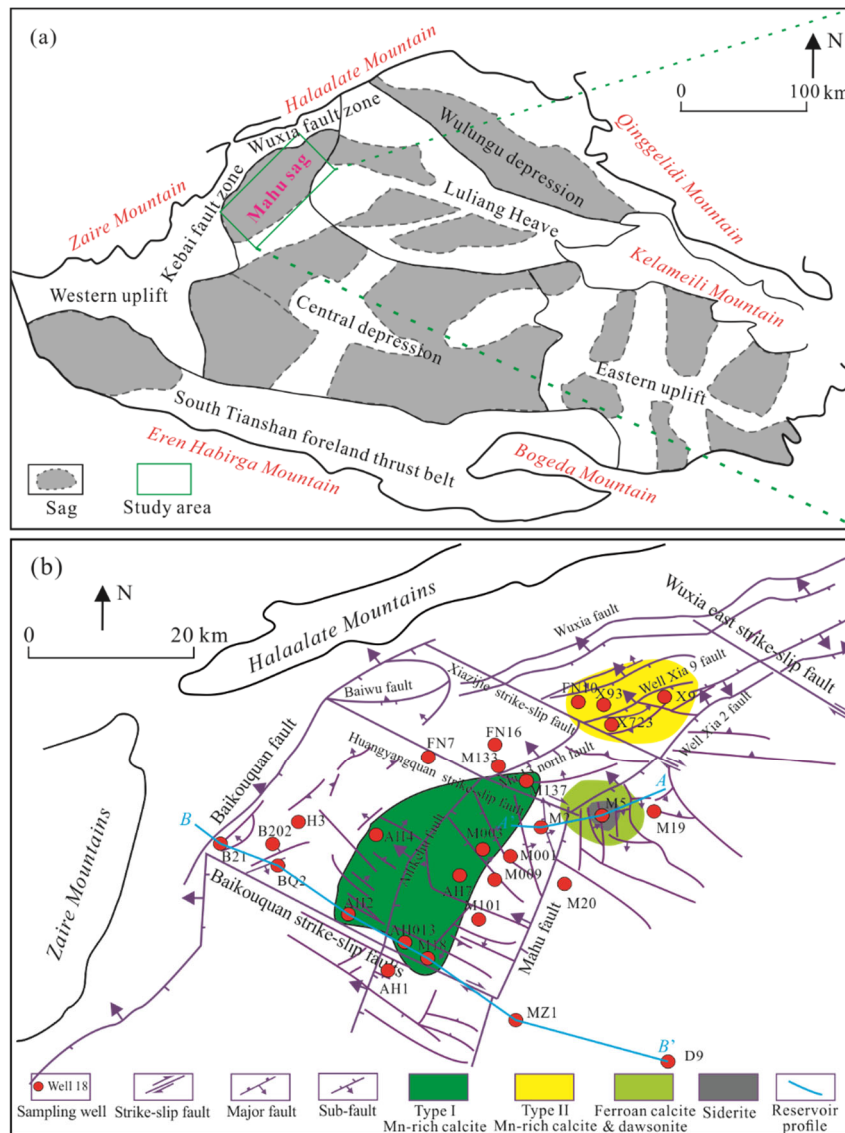
Figure 1. (a) The tectonic units in the Junggar Basin and the location of the study area (the slope of Mahu sag); (b) structural map (modified after Chen et al., 2015) and the location of wells in the study area.

samples, 216 whole-rock bulk and clay fraction mineralogy analyses, 489 particle analysis data, and the oil test results of 18 wells were obtained from Geological Scientific Research Institute of the PetroChina Xinjiang Oilfield Company.

2.1   Sample Locations

These typical samples were distributed near different fractures and collected from one bed on the basis of different phase sequence layers. Therefore, 169 conglomerate samples were collected from bottom and middle of phase sequence layers. Forty-five sandstone samples were collected from the top of phase sequence layers and sandstone section.

2.2   Petrographic Description

A total of 192 blue epoxy resin-impregnated thin sections from 21 core wells were provided for mineralogy and diagenesis analyses. These thin sections were also partly stained with Alizarin Red-S and potassium ferricyanide solutions to differentiate the carbonate cement types. In order to check the validity of the

collected rock composition data, the framework particles and authigenic minerals of 30 conglomerate samples and 30 sandstone samples thin sections were confirmed by averaging 300-point counts per thin section.

One hundred and twenty-six blue epoxy resin-impregnated thin sections were observed under a Zeiss Axioscope A1 APOL digital transmission microscope with 5×, 10×, 20×, and 50× lenses to recognize different mineral compositions as well as petrographic and diagenetic features and quantity the cement content. Under 10× lenses, 45 blue epoxy resin-impregnated thin sections were determined by 9 photo-micrographs per thin section to qualify the content of carbonate cements by Image-Pro Plus 6.0 software.

Forty-six samples were selected for cathodoluminescence analyses by Zeiss microscope with a CL8200 MK5 detector. The acceleration voltage and electric current were 10 kV and 250 μA, respectively. The exposure times were 8 and 12 s at 10× and 20× lenses.
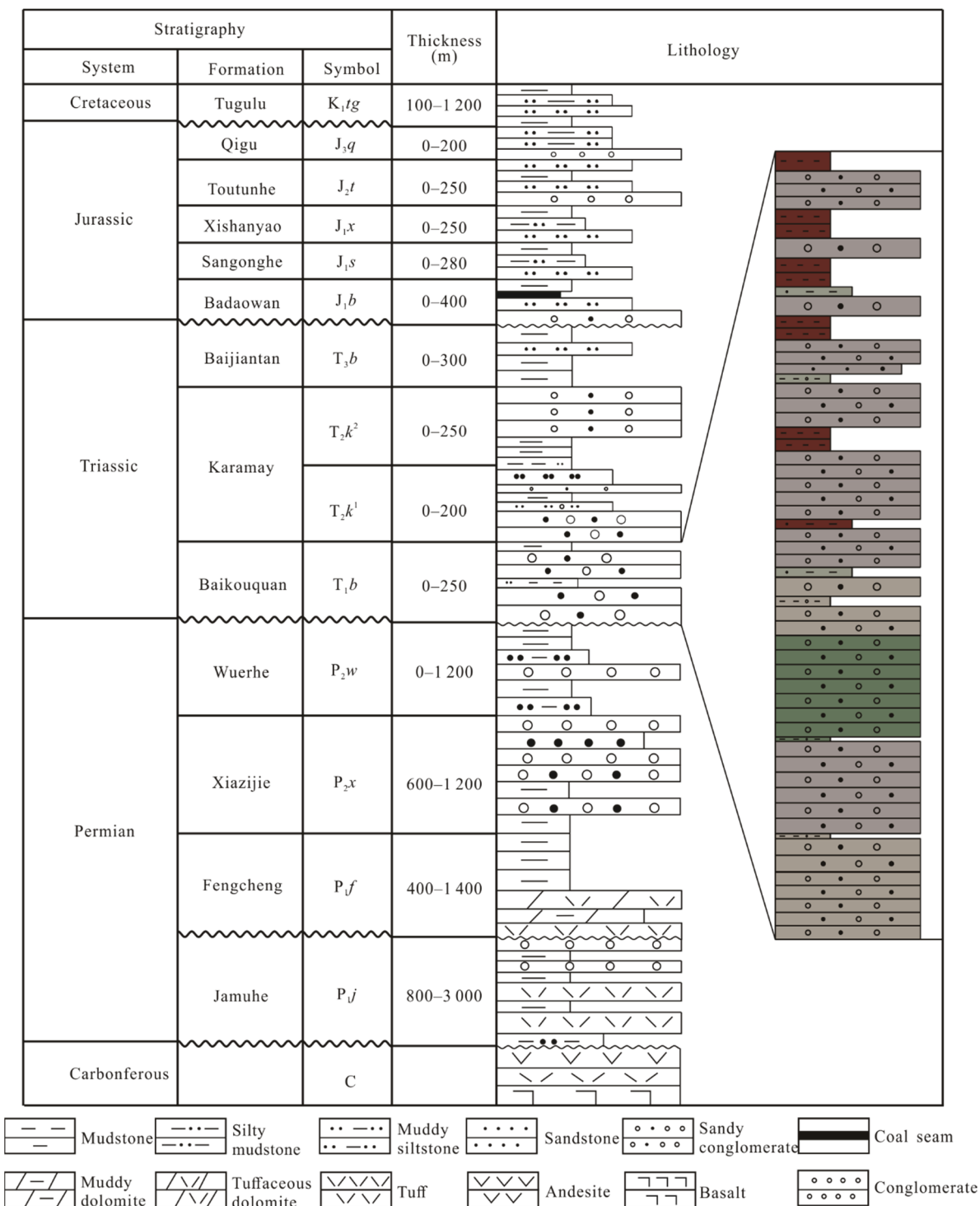
Figure 2. Generalized stratigraphic column of the study area.

2.3 Fluid Inclusion Analysis

Twenty-two samples from 7 core wells were prepared as thick double polished thin section for fluid inclusion analyses and fluorescence analyses. The micro thermometry of aqueous fluid inclusions was analyzed by a petrographic microscope equipped with Linkam THMSG 600 heating-cooling stage. The aqueous fluid inclusions were cooled to -20 ℃ at first, and then the heating rate was 10 ℃/min lower than 50 ℃, 5 ℃/min between 50 and 80 ℃, and then reduced to 0.2 ℃/min when approaching phase transformation. The measurement accuracy of

homogenization temperature is ±1 ℃.

2.4 Carbon and Oxygen Isotope Analysis

Forty sandy conglomerate samples from 7 core wells were selected for stable carbon and oxygen isotope analyses. The samples were analyzed by a Gas Bench and Delta V Plus isotope ratio mass spectrometer at the Institute of Geology and Geophysics, Chinese Academy of Sciences. The precision of $\delta^{13}C$ was less than 0.1‰ and $\delta^{18}O$ was less than 0.15‰, and the carbon and oxygen stable isotope data were presented in the δ notation

relative to the V-PDB standards.

2.5 Elements Analysis

Twenty-two typical samples from 7 core wells were selected for Electric Probe Microanalysis point analysis by JEOLJXA-8230 microanalyzer at the Ocean University of China. The weight percentage for the oxides of Fe, Mg, Ca, Mn, Sr, Al, Na, etc. in carbonate minerals was analyzed at 219 points. The acceleration voltage and electric current were 20 kV and 1×10^{-8} A, respectively. The spot size was from 3 to 10 μm. The accuracy of major elements and trace elements was 1 wt.% and 3 wt.%, respectively.

3 RESULTS

3.1 Reservoir Lithologies

According to the grading analysis, the studied T_1b glutenite reservoirs are mainly composed of 70.33% fine- to medium-grained conglomerates, followed by 16.06% coarse-grained sandstones. Mudstone, siltstone and fined-grained sandstone account for 13.61% (Fig. 3a). The gravel compositions of the conglomerates are mainly intermediate-acidic extrusive rocks (felsite and andesite), tuff, granite and some metamorphic rocks (Fig. 3b). Importantly, there is no carbonate rock clast in the study area. The sandstone of the T_1b is mainly litharenite and feldspathiclitharenite according to the Folk et al. (1970) classification scheme (Fig. 3c). The petrographic investigation shows that the

quartz content is 2% to 45%, with an average of 20.1%, the feldspar content is 2% to 32%, with an average of 14.9%, and the rock fragment content is 23% to 97%, with an average of 65.2%. The matrix is mud-based, and intergranulartuff accounts for up to 2% to 18%, with an average of 6.37%, which are mainly caused by sedimentation and sediment sources. The compositional maturity of sandstone is 0.02 to 0.82, with an average of 0.27. According to Petroleum and Nature Gas Industry Standard of the People's Republic of China (SY/T 5453-2018) (NEA, 2018), the standard deviations of sandstone and glutenite particle size range from 0.75 to 2.61 (with an average of 1.72) and 0.98 to 2.74 (with an average of 1.87), respectively, which indicates fair-poorly to poorly sorted (Fig. 3d).

3.2 Characteristics of the Carbonate Cements

3.2.1 Chemical composition

The contents of CaO, FeO, MgO and MnO (wt.%) are plotted as triangular diagrams (Fig. 4a). According to the classification from Dos Anjos et al. (2000) and Morad (1998), four types of carbonate cements can be recognized from the triangular diagram, and they are siderite, dawsonite, Mn-rich calcite and ferroan calcite (Fig. 4a).

3.2.2 Mn-rich calcite

Mn-rich calcite cement is characterized by abundant Mn (Mn up to 11.40 wt.%; average of 5.95 wt.%) but low ferroan
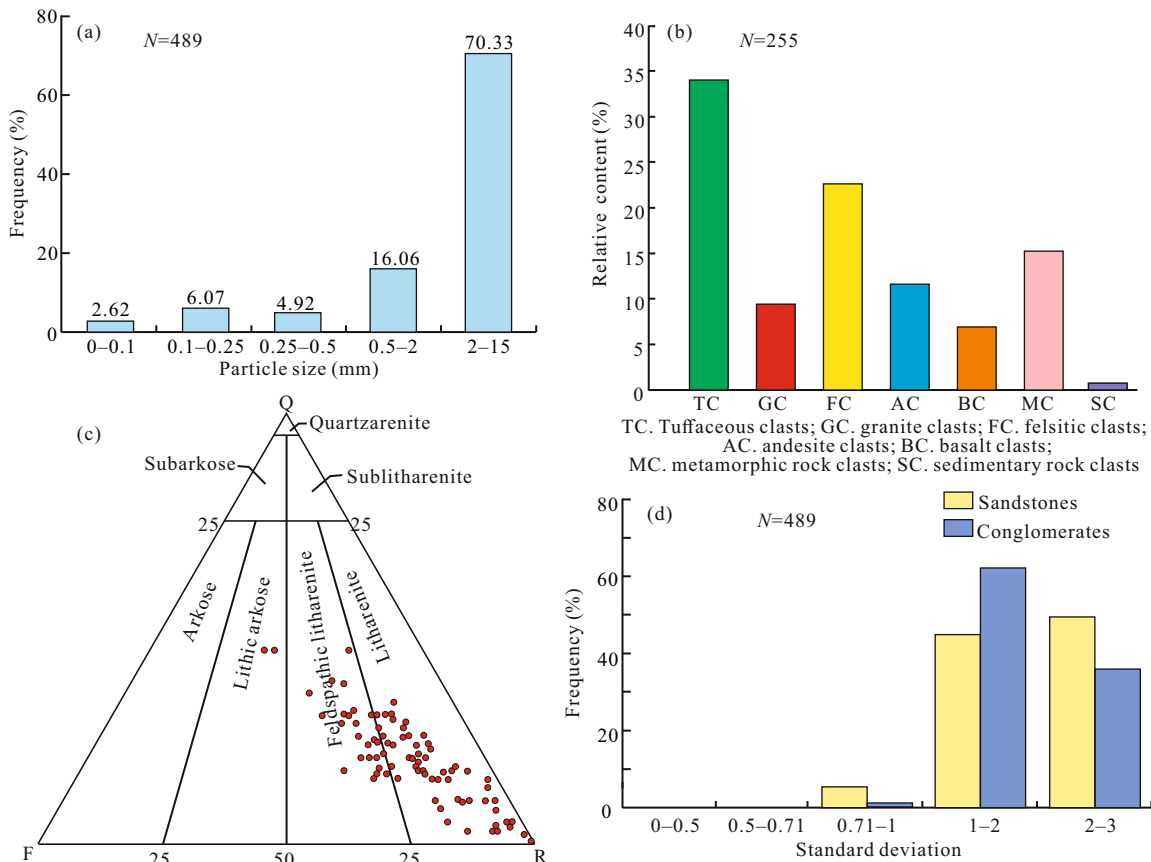

Figure 3. (a) Histogram showing the particle size in T_1b; (b) histogram showing the relative contents of the rock fragments in T_1b; (c) ternary plot showing rock compositions of the T_1b sandstone reservoir in Mahu sag (refer to the sandstone classification standard of Folk et al., 1970); (d) histogram showing the standard deviations of sandstones and conglomerates in T_1b. Q. Quartz; F. feldspar; R. rock fragments.
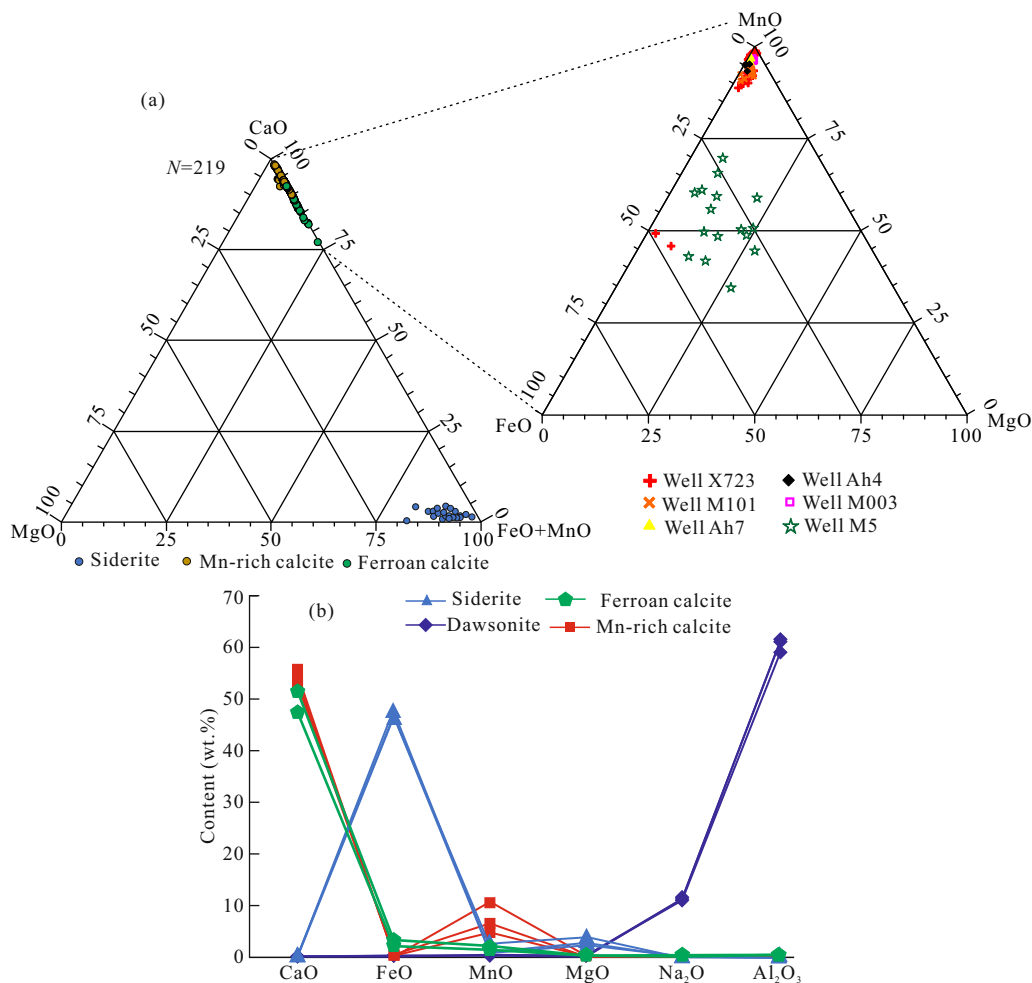
Figure 4. Chemical compositions of carbonate cements in glutenite reservoir of T_1b on the slope of Mahu sag. (a) Ternary plot showing weight proportions of Ca, Mg, Fe and Mn, showing carbonate cements composed of siderite, Mn-rich calcite and ferroan calcite; (b) line chart showing the change of elements in carbonate minerals.

Table 1   EPMA results for different types of carbonate cements in the T_1b glutenite reservoirs

Carbonate types	Element content (wt.%)									
	Ca		Mg		Fe		Mn		Na	Al
	Range	Average	Range	Average	Range	Average	Range	Average	Average	Average
Mn-rich calcite	45.7–54.4	52.49	0.01–0.3	0.13	0.05–1.5	0.37	2.43–11.4	5.95	-	-
Ferron calcite	45.9–56.5	52.65	0.08–1.0	0.42	1.17–3.2	1.59	0.5–2.9	1.18	-	-
Siderite	0.2–0.6	0.44	1.8–5.6	2.43	42.8–48.5	45.4	0.6–2.5	1.36	-	-
Dawsonite	-	0.39	-	0.008	-	0.013	-	0.01	10.94	56.79

components (Fe up to 1.53 wt.%; average of 0.37 wt.%) (Table 1, Fig. 4b). It mainly occurs as pore-filling crystals or scattered patchy crystals, with some fissure-filling crystals (Figs. 5a–5b). Mostly, the Mn-rich calcite is filled in particle-dissolution pores and intergranular-dissolution pores. It shows red color in the stained thin sections and light-yellow luminescence (Figs. 5c–5d). The size ranges from 10–100 μm. The content is approximately 6.38% (up to 16.8%).

3.2.3   Ferroan calcite

Ferroan calcite is characterized by relatively abundant ferroan (Fe up to 3.20 wt.%; average of 1.59 wt.%) but low Mn components (Mn up to 2.90 wt.%; average of 1.18 wt.%) (Table

1, Fig. 4b). It mainly appears as poikilotopic blocky crystals filled in intergranular pores and particle fringe solution pores (Figs. 5e–5f). It is characterized by a purple to pink color in the stained thin sections and dark orange luminescence under cathodeluminescence (Fig. 5g). The size of those rhombic crystal ranges from 20–200 μm. The content of ferroan calcite is 4.67% (up to 10.08%).

3.2.4   Siderite

Siderite is characterized by high Fe content (42.8 wt.% to 48.5 wt.%, average of 45.4 wt.%) and Mg content (1.8 wt.% to 5.6 wt.%, average of 2.43 wt.%) (Table 1, Fig. 4b). Siderite fills in the primary intergranular pores, characterized by dark

spherulite crystal rims around the detrital grains, as very fine grained (Fig. 5h). The size of the siderite is approximately 2 μm, and the surface is porous (Fig. 5i). It was visibly engulfed by ferroan calcite (Fig. 5j). The content of siderite is approximately 10.32% (up to 15.44%).

3.2.5 Dawsonite

In the research area, the distribution of dawsonite is limited, and the content is much less abundant than ferroan calcite and Mn-rich calcite. Dawsonite was characterized by high Na_2O and Al_2O_3 contents (Table 1, Fig. 4b). Under light optics, dawsonite is distinguished by acicular habit, typically forming bundles, tuffs and vermicules (Gao et al., 2005; Baker et al., 1995). In this study area, dawsonite is characterized by radiate and bunchy fills in the secondary pores and partly replaces feldspar (Figs. 5k–5l).
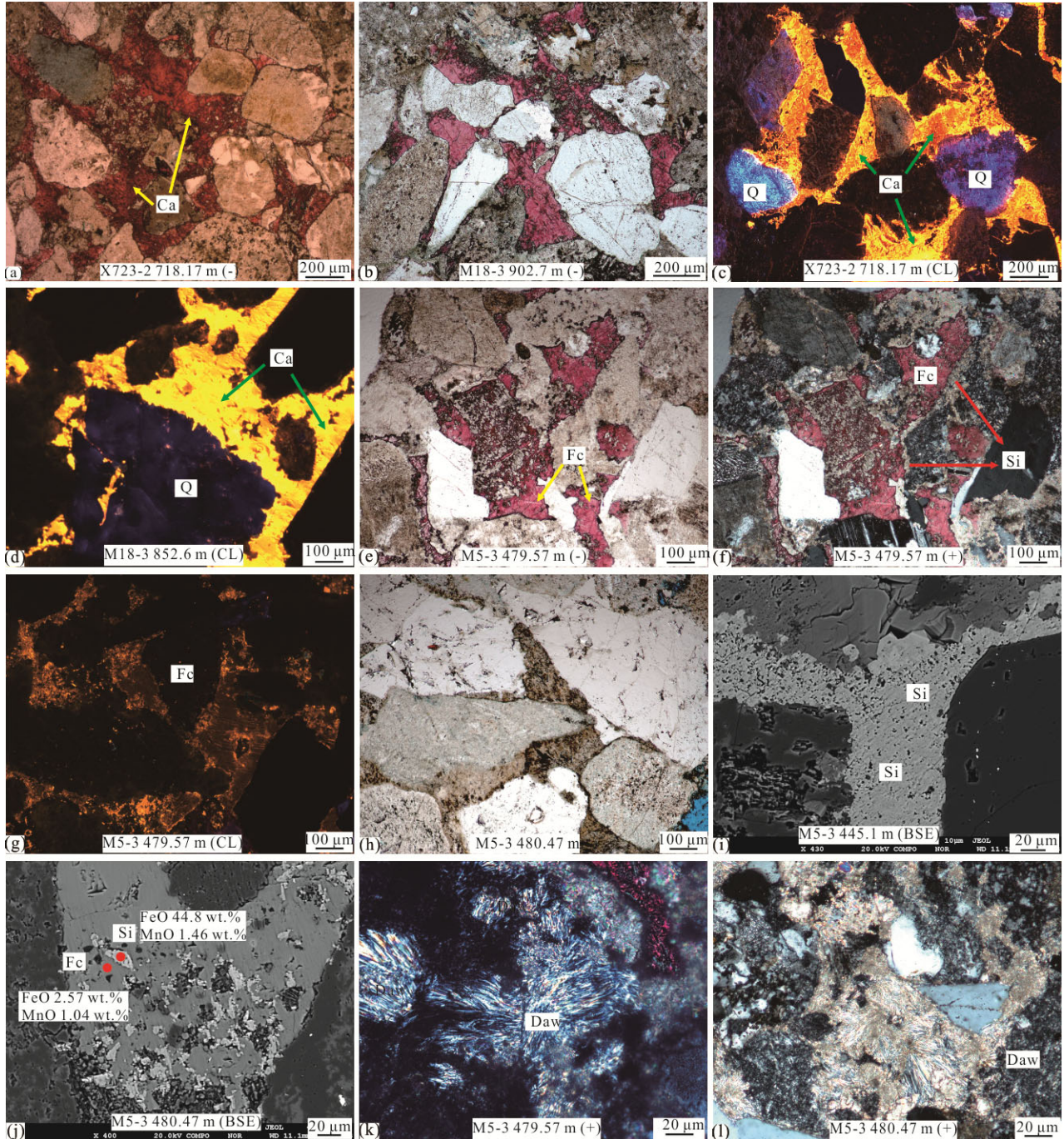

Figure 5. Photomicrographs of carbonate cement features in the T₁b sandy conglomerate. (a), (b) Mn-rich calcite filled in intergranular pores and rock fragments dissolution pores; (c), (d) Mn-rich calcite shows light yellow luminescence under cathodeluminescence; (e), (f) ferroancalcites filled in intergranular pores and siderite dissolution pores; (g) ferroan calcite shows dark orange luminescence under cathodeluminescence; (h), (i) siderite filled in intergranular pores and the surface of it is porous; (j) siderite engulfed by ferroan calcite; (k), (l) dawsonite characterized by radiate. Si. Siderite; Ca. Mn-rich calcite; Fc. ferroan calcite; Q. quartz; Daw. dawsonite.

3.3   Fluid Inclusions in Carbonate Cements

Aqueous fluid inclusions were found in Mn-rich calcite (Fig. 6a) and ferroan calcite (Fig. 6b). The diameter of these aqueous fluid inclusions is approximately 2.3 to 7.1 μm. The measured homogenization temperatures for aqueous fluid inclusions in ferroan calcite and Mn-rich calcite are shown in Table 2.

The measured temperatures of aqueous fluid inclusions in ferroan calcite range from 73.2 to 90.8 ºC. The measured temperatures of aqueous fluid inclusions in Mn-rich calcite range from 92.6 to 116.4 ºC. In addition, only hydrocarbon inclusions showing blue-white luminescence were observed in Mn-richcalcite (Figs. 6c, 6d).
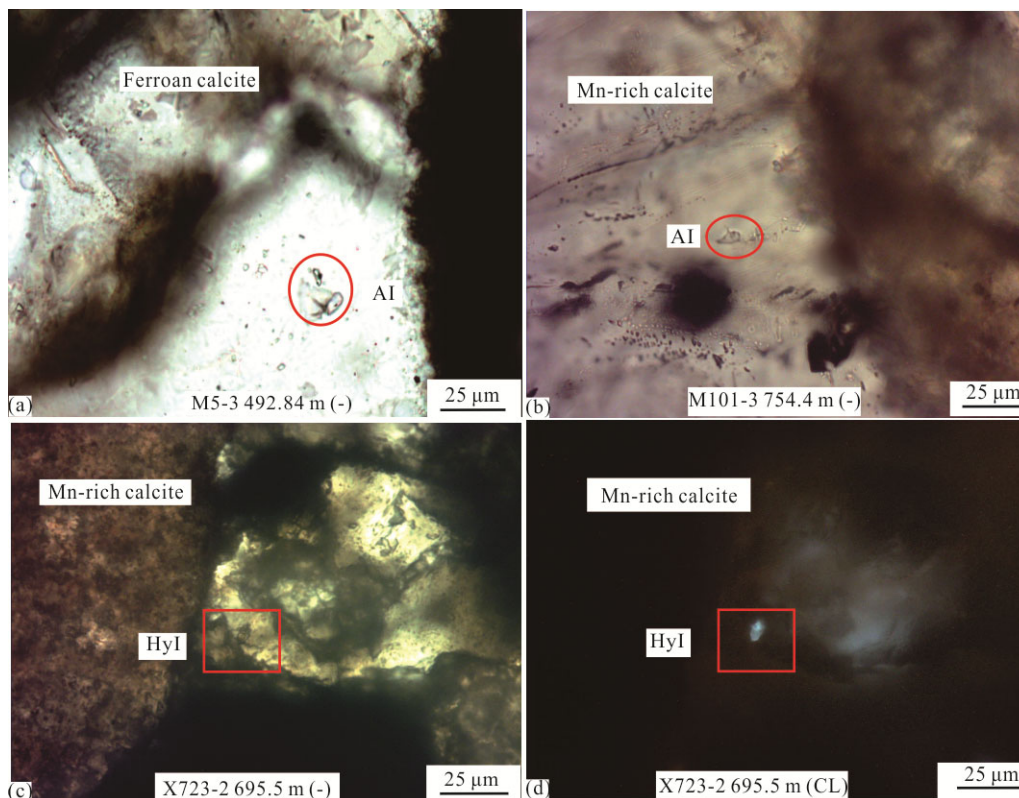

Figure 6. Photomicrographs of inclusions under transmitted light at room temperature in glutenite reservoirs of T_1b. (a) Aqueous inclusions in pore-filling ferroan calcite; (b) aqueous inclusions in pore-filling Mn-rich calcite; (c) hydrocarbon inclusion in Mn-rich calcite; (d) hydrocarbon inclusion in Mn-rich calcite shows blue-white luminescence under cathodeluminescence. AI. Aqueous fluid inclusion; HyI. Hydrocarbon inclusion.

Table 2   Microthermometry data of the fluid inclusions in the T_1b reservoir. T_h. homogenization temperature

Well	Depth (m)	Host mineral	Size (μm)	Types	T_h (ºC)
FN10	2 746.0	Mn-rich calcite	3.6	Aqueous	109.3
FN10	2 746.0	Mn-rich calcite	5.72	Aqueous	112.2
FN10	2 746.0	Mn-rich calcite	4.56	Aqueous	102.6
M101	3 754.4	Mn-rich calcite	2.3	Aqueous	98.3
M101	3 754.4	Mn-rich calcite	3.1	Aqueous	101.3
M101	3 754.4	Mn-rich calcite	3.92	Aqueous	92.6
M101	3 754.4	Mn-rich calcite	4.71	Aqueous	108.4
X723	2 695.1	Mn-rich calcite	3.2	Aqueous	110.5
X723	2 695.1	Mn-rich calcite	3.6	Aqueous	116.4
X723	2 695.1	Mn-rich calcite	2.8	Aqueous	109.2
X723	2 695.1	Mn-rich calcite	2.6	Aqueous	108.5
M5	3 492.84	Ferroancalcite	4.35	Aqueous	81.4
M5	3 492.84	Ferroancalcite	3.1	Aqueous	86.9
M5	3 492.84	Ferroancalcite	3.76	Aqueous	73.2
M5	3 492.84	Ferroancalcite	3.68	Aqueous	82.6
X723	2 686.4	Ferroancalcite	4.15	Aqueous	79.3
X723	2 686.4	Ferroancalcite	3.2	Aqueous	76.5
X723	2 686.4	Ferroancalcite	7.1	Aqueous	90.8

Table 3 Mineralogical and isotopic composition of carbonate cements in T_1b glutenite reservoirs

Well	Depth (m)	Rock types	Carbonate minerals	Content (%)	$\delta^{13}C_{PDB}$ (‰)	$\delta^{18}O_{PDB}$ (‰)	Temperature (℃)
AH-7	3 612.20	Glutenite	100%Ca	1.99	-32.31	-20.40	106.80
AH-4	2 884.00	Glutenite	100%Ca	3.27	-53.46	-21.01	113.13
M-18	3 852.60	Glutenite	100%Ca	1.74	-37.90	-18.92	92.54
M-18	3 872.00	Glutenite	100%Ca	1.78	-50.18	-20.27	105.46
M-18	3 902.70	Glutenite	100%Ca	5.46	-50.87	-19.30	96.08
M-101	3 754.40	Glutenite	100%Ca	4.39	-54.99	-20.40	106.76
M-137	3 254.50	Glutenite	100%Ca	2.01	-54.40	-22.10	125.33
M-003	3 465.86	Glutenite	100%Ca	3.86	-27.04	-19.22	95.29
M-003	3 466.46	Glutenite	100%Ca	3.14	-31.26	-19.32	96.28
M-003	3 468.60	Glutenite	100%Ca	2.23	-32.27	-19.63	99.13
FN-10	2 679.50	Glutenite	100%Ca	6.50	-10.30	-21.80	121.85
FN-10	2 746.00	Glutenite	100%Ca	1.35	-5.20	-20.80	110.90
FN-10	2 772.90	Glutenite	100%Ca	4.55	-2.90	-23.40	141.51
FN-10	2 775.80	Glutenite	100%Ca	6.31	-2.90	-20.70	109.85
X-723	2 677.00	Glutenite	90%Ca+10%Fc	4.98	-15.40	-21.00	113.02
X-723	2 680.50	Sandstone	100%Fc	2.10	2.0	-18.73	89.51
X-723	2 686.40	Sandstone	100%Fc	3.20	8.80	-18.48	88.63
X-723	2 695.10	Glutenite	75%Ca+25%Fc	6.40	-8.73	-19.71	99.91
X-723	2 695.50	Glutenite	75%Ca+25%Fc	9.20	-11.50	-22.20	126.51
X-723	2 700.10	Glutenite	75%Ca+25%Fc	6.90	-13.36	-19.70	99.88
X-723	2 711.25	Sandstone	85%Ca+15%Fc	4.41	-17.30	-22.00	124.16
X-723	2 716.20	Glutenite	85%Ca+15%Fc	3.34	-17.40	-22.10	125.33
X-723	2 718.17	Glutenite	90%Ca+10%Fc	2.70	-18.80	-21.90	123.00
X-723	2 722.50	Glutenite	90%Ca+10%Fc	5.70	-19.94	-21.12	114.29
M-5	3 444.75	Glutenite	100%Si	10.32	-0.07	-12.33	44.33
M-5	3 445.10	Glutenite	100%Si	9.65	0.25	-12.21	43.63
M-5	3 479.57	Glutenite	95%Fc+5%Daw	11.31	-12.37	-18.97	93.01
M-5	3 480.47	Glutenite	85%Fc+12%Si+3%Daw	4.28	-5.06	-14.75	59.74
M-5	3 490.44	Glutenite	90%Fc+5%Si+5%Daw	3.98	-2.62	-18.62	89.84
M-5	3 492.84	Glutenite	100%Fc	5.47	-3.20	-18.03	84.73
M-5	3 495.90	Glutenite	90%Fc+10%Si	5.22	-2.92	-18.32	87.21
M-5	3 518.90	Glutenite	100%Fc	2.58	-2.43	-17.82	82.94

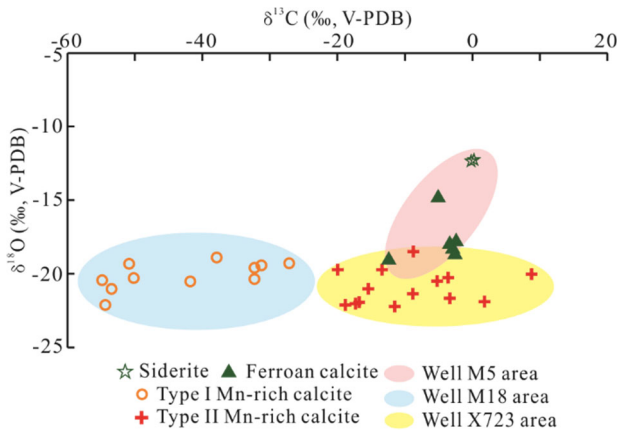Ca. Mn-rich calcite; Fc. ferroan calcite; Si. siderite; Daw. dawsonite.

Figure 7. Carbon and oxygen isotopic characteristics of carbonate cements in the Mahu sag slope area.

3.4 Carbon and Oxygen Isotope Compositions

The carbon and oxygen isotope compositions of carbonate cements were analyzed from 40 glutenite samples (Table 3, Fig. 7). The contents of carbonate cement were counted with thin sections. The $\delta^{13}C$ values of Mn-rich calcite in the M18 Well area range from -54.99‰ to -1.66‰, and the $\delta^{18}O$ values range from -23.40‰ to -18.48‰. For siderite, the $\delta^{13}C$ values range from -0.07‰ to 0.25‰, while the $\delta^{18}O$ values range from -12.33‰ to -12.21‰. For ferroan calcite, the $\delta^{13}C$ values range from -12.37‰ to +8.8‰, while the $\delta^{18}O$ values range from -18.97‰ to -14.75‰. Data about dawsonite is not available owing to minor occurrence.

4 DISCUSSION

4.1 Timing of Carbonate Cement

The intergranular volume of glutenite, the homogenization

temperature of aqueous inclusions and isotopic data can be used to indicate the precipitation time of carbonate mineral (Yang et al., 2018). The intergranular volume of siderite-cemented glutenite is 27.7%. The intergranular volumes of ferron calcite and Mn-rich calcite are 18.3% and 12.9%, respectively. The intergranular volume of glutenite decreases following the paragenetic sequence of carbonate cementation.

The formula given by Friedman and O'Neil (1977) to calculate the precipitation temperature of calcite is as follow

$$1\,000 \times \ln \alpha_{calcite\text{-}water} = 2.78 \times 10^6 / T^2 - 2.89 \qquad (1)$$

where $\ln \alpha_{calcite\text{-}water} = \delta^{18}O_{calcite} - \delta^{18}O_{water}$. This model has been proved to be appropriate for the temperature from 0 to 500 ºC (Friedman and O'Neil, 1977).

The formula proposed by Carothers et al. (1988) to calculate the precipitation temperature of siderite is as follow

$$1\,000 \times \ln \alpha_{siderite\text{-}water} = 3.13 \times 10^6 / T^2 - 3.50 \qquad (2)$$

where $\ln \alpha_{siderite\text{-}water} = \delta^{18}O_{siderite} - \delta^{18}O_{water}$. Thereinto, $\delta^{18}O_{calcite}$ is the tested isotope value, and $\delta^{18}O_{water}$ is the value of the original formation water. Thus, in order to calculate the precipitation temperature of carbonate cements by the oxygen isotope fractionation formal, $\delta^{18}O_{water}$ must be established first. According to the data of aqueous inclusion, the precipitation temperature of 5 samples can be acquired. Meanwhile, the oxygen isotope of the 5 samples can also be determined. In this way, the calculated $\delta^{18}O_{water}$ values are -7.22‰– -5.93‰ (SMOW), with an average of -6.54‰ (SMOW). Finally, the results of the Formula (1) will be used as the formation temperature of the ferran calcite cements ranging from 59.74 to 93.01 ºC, that of Mn-rich calcite ranging from 92.54 to 141.51 ºC (Table 3). And on the basis of the Formula (2), the formation temperature of siderite cements is approximate 44 ºC (Table 3). Dawsonite is associated with ferroan calcite. Therefore, it is believed to be the simultaneous product of ferroan calcite.

Combined with the burial history, it can be speculated that the formation time of siderite ranges from 231 to 220 Ma, the formation time of ferroan calcite and dawsonite range from 185 to 142 Ma, the formation time of Mn-rich calcite ranges from 148 to 105 Ma.

4.2   Origin and Genesis of Carbonate Cements

Carbonate cements have several potential carbon sources, such as internal, external and mixed sources. The $\delta^{13}C$ values of carbonate cements have been used to identify the origin of carbon (Kong et al., 2017; El-Khatri et al., 2015; McBride and Parea, 2001; Rosenbaum and Sheppard, 1986). Generally, the positive $\delta^{13}C$ values suggest the carbon from seawater (Anderson and Arthur, 1983), residual CO_2 from methanogenesis (Naehr et al., 2007; Gieskes et al., 2005), or early derivation of dissolved carbonate during recrystallization of detrital limestone (Bath et al., 1987). In contrast, the negative $\delta^{13}C$ values of carbonate cements may indicate the carbon from thermal maturation organic matter (Yang et al., 2018; Irwin et al., 1977), biogenic methane (Whiticar, 1999), thermogenic methane (Sackett and Chung, 1979), or oil fraction (Roberts and Aharon, 1994). Combined with the precipitation temperature calculated via oxygen isotope data, the

origin and genesis of carbonate cements can be determined.

Our carbonate cementation samples have extremely negative $\delta^{13}C$ values and positive $\delta^{13}C$ values for the carbonate cements. This outcome may reflect a variety of carbon sources and complex diagenesis mechanisms.

4.2.1   Source of CO_2 associated with siderite

As revealed by the characteristics of petrology and geochemistry, siderite is uniphase and most likely precipitated in a single diagenetic environment. On the one hand, most observed siderite falls on a linear trend of 0–10% $MgCO_3$, 0–10% $CaCO_3$ and 85%–95% $FeCO_3$ (Fig. 4a) with a lack of samples in the range of 75%–85% $FeCO_3$. In addition, siderite is also enriched in a certain amount of Mn, the content of which can reach 2.5 wt.%. Therefore, its composition is characteristic of early precipitation from meteoric water (Rossi et al., 2001; Mozley, 1989). The relatively high intergranular volumes of siderite (20% to 30%, Figs. 5k–5m) also suggest a relatively shallow depth of precipitation before compaction. The stable isotope data of siderite are also of interest. The $\delta^{13}C$ values for pure siderite cementation samples close to 0 are indicative of a meteoric water source for CO_2 (Bath et al., 1987). The negative $\delta^{18}O$ values (-12.33‰ to -12.21‰) must reflect the predominance of meteoric origin waters in the early diagenetic stage. However, the distribution of siderite is quite limited, which reveals that the influence of meteoric water on the research area is also limited.

4.2.2   Source of CO_2 associated with ferroan calcite

The $\delta^{13}C$ values of most ferroan calcite cements range from -12.37‰ to -2.43‰ (Fig. 8). The range of carbon isotopic data of ferroan calcite is very close to that of dawsonite, which has been confirmed to be formed in an inorganic CO_2 background and related to magmatic activity (Baker et al., 1995). The $\delta^{13}C$ values may indicate that the carbon source of ferroan calcite is mainly sourced from CO_2 thermal fluid of magmatic mantle origin but mixed with a small amount of decarboxylation of organic matter (Gao et al., 2005; Baker et al., 1995). Some special minerals can be used directly to determine the source of CO_2 (Hu, 2016). For example, dawsonite is considered to be a symbolic mineral under high mantle inorganic CO_2 partial pressure (Hu, 2016), which was found to be accompanied by ferroan calcites in the Well M5 area. Previous studies have suggested that the authigenic dawsonite is the result of a reaction between Na^+-rich alkaline waters, an influx of CO_2
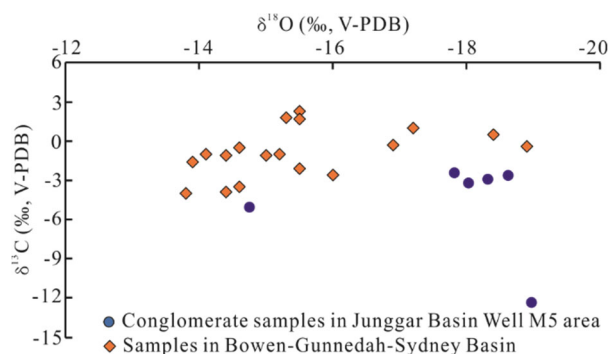

Figure 8. Plot showing the stable carbon and oxygen isotope characteristics for ferroan calcite in Well M5 area.

and an indigenous source of aluminum (Worden, 2006; Gao et al., 2005). In this study area, dawsonite was mainly formed by replacing sodium aluminosilicate minerals, such as feldspar with aqueous solutions rich in CO_2.

However, what is the origin of the inorganic mantle CO_2, and how does it move to the reservoir? It is generally believed that the Junggar Basin entered a relatively stable intra-continental evolution stage in the Triassic, and the large-scale magmatic activity basically stopped (Chen et al., 2002). However, Xu et al. (2008) found that Jurassic basalt outcrop in the western Junggar Basin belonged to an alkaline basalt series, which indicated the eruption of mantle-derived magma (Guo et al., 2010). In addition, we found that the Well M5 area is in the boundary zone of the Huangyangquan strike-slip fault and Mahu fracture, both of which are high-angle deep-large fractures (Fig. 9) and provide a good migration channel for inorganic mantle CO_2. The $\delta^{18}O$ isotope-based temperature of ferron calcite is 59.74 to 93.01 ℃. Combined with the burial history, the formation time of ferron calcite and dawsonite is from Early Jurassic to Middle Jurassic, which also has a good matching relationship with the time of magmatic activity.

In other words, mantle CO_2 is considered to be a main source of carbonic acid for ferron calcite, while the dissolution of pre-existing siderite provides the necessary cations for ferron calcite. As is mentioned before, T_1b reservoir experienced two-stage hydrocarbon-charging: Late Triassic–Early Jurassic and Late Jurassic–Early Cretaceous. The first hydrocarbon-charging occurred before the formation of ferron calcite but after the formation of siderite, which resulted in the dissolution of siderite. The Fe^{2+} from dissolving siderite is the main source of ferroan-cations.

In addition, we can observe that there is a sample of carbon isotope values within the range of organic decarboxylation origin (Fig. 8), and the Mn content of this sample is 1 wt.% to 3 wt.% higher than that of other samples. Therefore, it is inferred that its formation is associated with the organic CO_2 of organic matter decarboxygenation.

4.2.3 Source of CO₂ associated with Mn-rich calcite

Mn-rich calcite is the most abundant carbonate cement in the study area. The Mn-rich calcite can be divided into two groups according to the carbon isotope compositions. The carbon isotope compositions of Type I Mn-rich calcite show the most depleted $\delta^{13}C$ values ranging from -54.99‰ to -27.04‰, while that of Type II Mn-rich calcite display light $\delta^{13}C$ values ranging from -21.46‰– -1.66‰. The Mn content of Type I Mn-rich calcite (Fig. 5d) is 2.43 wt.% to 5.58 wt.%, with an average of 3.85 wt.%, while that of Type II Mn-rich calcite (Fig. 5c) is 3.23 wt.% to 11.41 wt.%, with an average of 6.17 wt.%. However, the oxygen isotope values of both Mn-rich calcites have approximately the same range. Therefore, the two types of Mn-rich calcites have different CO_2 sources and precipitation mechanisms.

4.2.3.1 Type I Mn-rich calcite

Type I Mn-rich calcite is mainly distributed in the Well M18 area, west of the study area, which is characterized by depleted $\delta^{13}C$ values (-54.99‰– -27.04‰). In comparison to the carbon isotope data of methane gas from the Xinjiang Oilfield, the $\delta^{13}C$

values of methane, ethane, propane and butane in natural gas are -47.83‰– -43.54‰, -31.87‰– -30.5‰, -30.54‰– -28.25‰ and -29.77‰– -27.78‰, respectively (Fig. 10). Previous studies proved that the carbon source mainly comes from CO_2 formed by methane thermochemical oxidation, with a small contribution of oxidation of minor C_{2+} and decarboxylation of organic acids (Hu et al., 2018). There are several natural gas areas in the Carboniferous and Permian of Mahu anticline, and the content of methane is 73%–92% (Pan et al., 2007), demonstrating that the source rocks in the Well M18 area have evolved to a high-mature stage and generated a large amount of natural gas. The natural gas provides a material basis for oxidation.

How is the methane transported to the reservoirs and how is it oxidized? The Ailikehu fracture in the Well M18 area, cutting off from the Carboniferous to the Triassic Karamay Formation (Chen et al., 2015), provides a channel for the upward migration of methane gas (Fig. 11) (Xu et al., 2014). Fluid advection is required to carry gaseous hydrocarbon from depth along such large-scale faults to the upper part of the sedimentary succession to get oxidized by the high valence Mn and Fe oxides (Hu et al., 2018; Suess et al., 1989). It is proved that the gaseous hydrocarbon is preferentially oxidized by high-valent Mn oxide (Hu et al., 2018). The EMPA analysis data indicate that compared with the MnO content, the FeO content of Type I Mn-rich calcite is much lower, no more than 0.2 wt.%. Thus, the precipitation of Type I Mn-rich calcite is related to methane oxidation by high-valence Mn. In addition, the time of second hydrocarbon-charging is 150–125 Ma, which is consistent with the formation time of Mn-rich calcite.
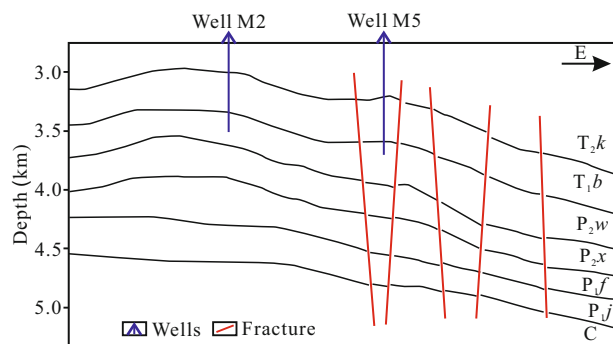

Figure 9. Profile showing reservoir development and fracture distribution from west to east on the western slope of the Mahu sag, and the profile position is shown in Fig. 1b (*A–A'*).
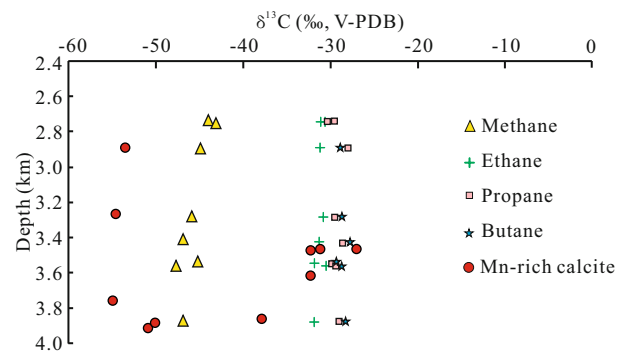

Figure 10. Carbon isotope of natural gas and Mn-rich calcite from Baikouquan reservoir.
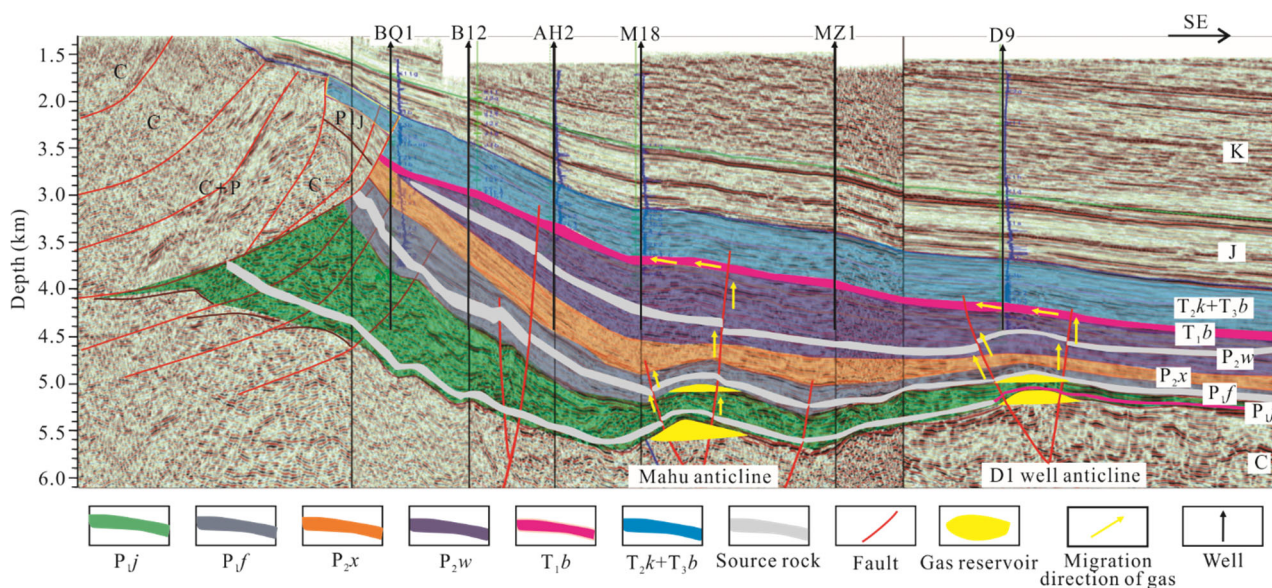
Figure 11. Profile showing reservoirs and faults and hydrocarbon distribution from northwest to southeastern, with the profile position in Fig. 1b (*B–B'*).

Therefore, it can be proved that Type I Mn-rich calcite is closely related to CO_2 formed by methane and minor C_{2+} thermochemical oxidation. From the distribution range of Type I Mn-rich calcite, the CO_2 fluid formed by gaseous hydrocarbon thermochemical oxidation has a wide influence on the reservoir.

4.2.3.2   Type II Mn-rich calcite

Type II Mn-rich calcite, with the $\delta^{13}C$ values showing a relatively important depletion (-21.46‰– -1.66‰), is mainly distributed in Well X723 area. The $\delta^{13}C$ values may reflect the carbon source from decarboxylation of organic acids (Sensula et al., 2006; Mack et al., 1991).

During Late Jurassic to Early Cretaceous Period, the hydrocarbon-bearing organic acid fluid was produced from the source rocks. During the peak generation of source rocks, with a significant volume of hydrocarbon-charging, the carboxylic acid anion was decarboxylated when the temperature of source rocks was over 135 ºC. The CO_2 from the decarboxylation of organic acids is easily combined with Ca^{2+} derived from dissolving feldspar to form calcite. Compared with Type I Mn-rich calcite, Type II Mn-rich calcite shows higher Mn content. The difference may be related to the source of Mn^{2+} and the formation mechanism of the two-type Mn-rich calcites. As is mentioned before, the precipitation of Type II Mn-rich calcite is associated with petroliferous fluid. During migration, the petroliferous fluid may interact with the Permian volcanic rocks, making these organic fluids rich in a large amount of Mn (Cao et al., 2007). Then, in the process of diagenesis, the Mn elements in hydrocarbon fluids can be transferred into calcite cements through the interaction between diagenetic fluid and rocks (Cao et al., 2007). In addition, based on the $\delta^{18}O$ values of Type II Mn-rich calcite, the calculated precipitation temperature ranges from 92.54 to 141.51 ºC. Combined with the burial history, the formation time of Type II Mn-rich calcite has a good matching relationship with the charging time of hydrocarbon. And the hydrocarbon inclusion showing blue-white fluorescence can be observed in Type II Mn-rich calcite. This means Type II Mn-rich calcite is formed at the time of the petroliferous-charging period.

Moreover, two samples showed positive $\delta^{13}C$ values, which were cemented by ferran calcite. At present, the $\delta^{13}C$ values of the lacustrine carbonate rocks are positive (Liu, 1998). Therefore, we believe that the ferran calcite samples, with positive $\delta^{13}C$ values (+2.0‰, +8.8‰), is attributed to the pure formation water precipitation (Cao et al., 2007). By counting the relative content of the ferran calcite and Mn-rich calcite in all samples, with increasing Mn-rich calcite content, the carbon isotopes are generally enriched in light carbon isotopes (Fig. 12). This result could explain the presence of the sample with slightly negative $\delta^{13}C$ values.

4.3   Paragenetic Sequence

Petrological observations will be combined with fluid inclusions and isotope analysis data to identify the relative time of each diagenesis and reconstruct the diagenesis history and oil and gas emplacement process of the T_1b glutenite reservoir. Cross-cutting relationship of cement, dissolution-filling relationship of diagenetic minerals can be used to infer paragenetic sequence (Guo et al., 2017). However, the petrological evidence about carbonate minerals is not convincing enough. Thus, the
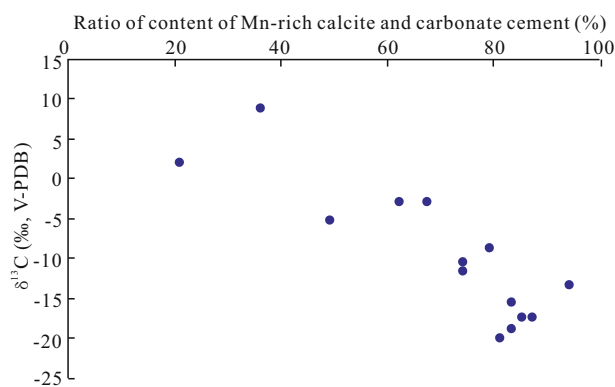

Figure 12. The relationship between the ratio of Mn-rich calcite to carbonate cement and $\delta^{13}C$ values in the Well X723 area.

homogenization temperature and oxygen isotope-based temperature were used to strengthen the paragenetic sequence of formation.

In addition to these carbonate cements, chlorite, analcime, kaolinite, quartz overgrowth and pyrite are also the authigenic minerals visible in reservoir (Fig. 13). The chlorite membrane is found around the detrital grains (Fig. 13a). The related study shows that the chlorite membrane is formed in syndiagenetic stage and the precipitation temperature is about 10 to 35 °C (Qu et al., 2017). Analcime is filling in intergranular pores and dissolves with feldspar and rock fragments (Fig. 13b). It has proved that the formation temperature is low, which is generally formed in early shallow-buried alkaline environment (Qi et al., 2015). Dissolution of feldspar and rock fragments is accompanied by the precipitation of kaolinite, pore-filling chlorite and quartz overgrowth. The kaolinite and pore-filling chlorite precipitate in secondary pores with chlorite membrane (Figs. 13a, 13c). The ferran calcite postdated the quartz overgrowth, and Mn-rich calcite postdated the authigenic kaolinite (Figs. 13d, 13e). The T_1b reservoir experienced two-period hydrocarbon-charging, of which the second-period is high maturity hydrocarbon-charging (Qi et al., 2015). The hydrocarbon inclusions in Mn-rich calcite show blue-white fluorescence (Fig. 6d), which indicates that the formation of Mn-rich calcite is slightly later than the second-stage hydrocarbon-charging. Pyrite postdated the Mn-rich calcite (Fig. 13f).

The scattered siderite surrounded by ferran calcite indicates that the ferran calcite postdated the siderite (Fig. 5j). Micro thermometric data of the aqueous fluid inclusions shows that homogenization temperature of aqueous inclusions of ferran calcite cements ranges from 73.2 to 90.8 °C, and that of Mn-rich calcite cements ranges from 92.6 to 116.4 °C. The oxygen isotope-based temperature shows that calculated precipitation temperature of siderite is about 44 °C, that of ferran calcite and Mn-rich calcite ranges from 59.74 to 93.01 °C, 92.54 to 141.51 °C, respectively. Dawsonite was considered to coincide with ferran calcite.

Therefore, the paragenetic sequence is established as follows: chlorite membrane precipitation→siderite/analcime precipitation→rock fragments/feldspar/siderite/analcime dissolution, authigenic kaolinite/pore-filling chlorite precipitation, quartz overgrowth→ferran calcite/dawsonite cementation→tuff/feldspar/rock fragments/ferran calcite dissolution→authigenic kaolinite/pore-filling chlorite precipitation→Mn-rich calcite precipitation→pyrite (Fig. 14) (Zhu et al., 2019).

4.4 Diagenetic Controls on Reservoir Quality

Although carbonate cements make the reservoir porosity decrease and reservoir physical property poor, the precipitation of large amounts of carbonate cements before the main compaction can protect the intergranular porosity, and the dissolution of early carbonate cements can improve the reservoir quality (Qiu et al., 2017; Wang et al., 2016). Thus, the reservoir influenced by different sourced CO₂ fluids and with different carbonate cements precipitated may also have different effects on the reservoir oil bearing property.

In the Well M5 area, the reservoir is mainly influenced by mantle-derived CO₂ fluid and minor meteoric water. Siderite and ferran calcite can be observed there. The quantitative statistics indicate that the siderite developed before the first hydrocarbon-charging reduces the thin-section porosity by 0.3%–15.44%, with an average of 3.49%. Subsequently, the siderite, feldspar
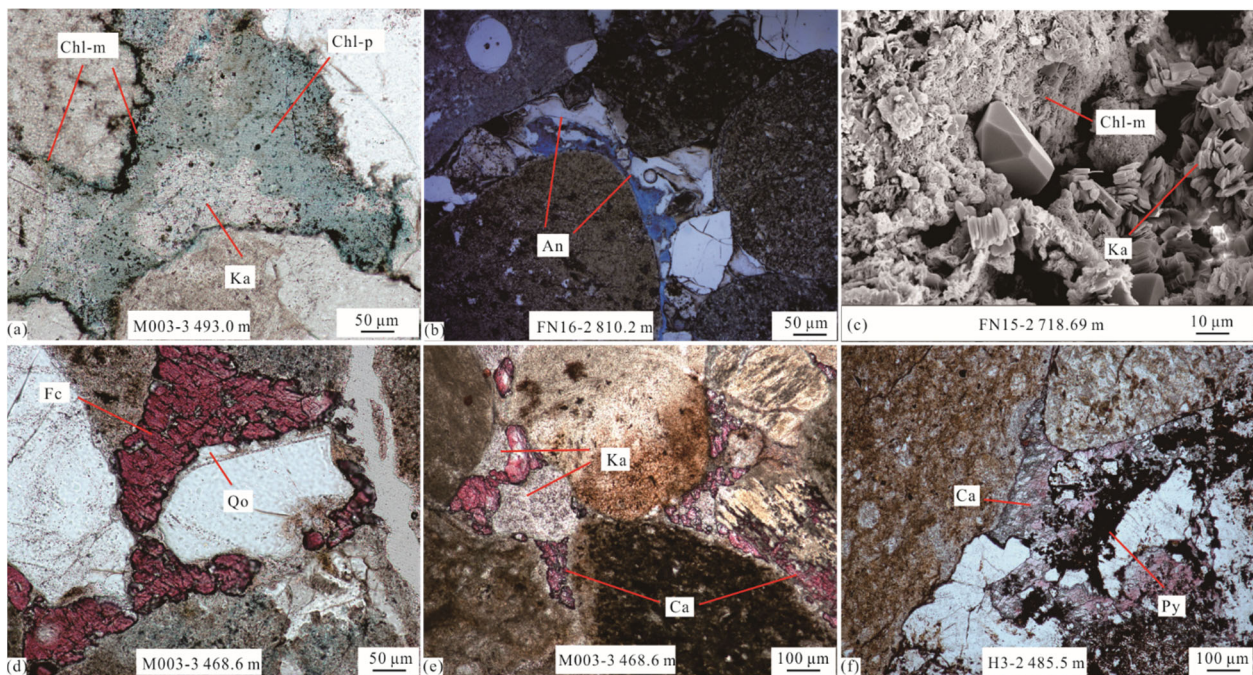

Figure 13. (a) Chlorite membrane precipitation around the grains, kaolinite and pore-filling chlorite filling in the secondary pores; (b) analcime precipitation and dissolution; (c) book-like kaolinite filling in the secondary pores; (d) quartz overgrowth replaced by ferran calcite; (e) kaolinite replaced by Mn-rich calcite; (f) Mn-rich calcite replaced by pyrite. Chl-m. Chlorite membrane; Chl-p. pore-filling chlorite; Ka. kaolinite; An. analcime; Qo. quartz overgrowth; Fc. ferran calcite; Ca. Mn-rich calcite; Py. pyrite.
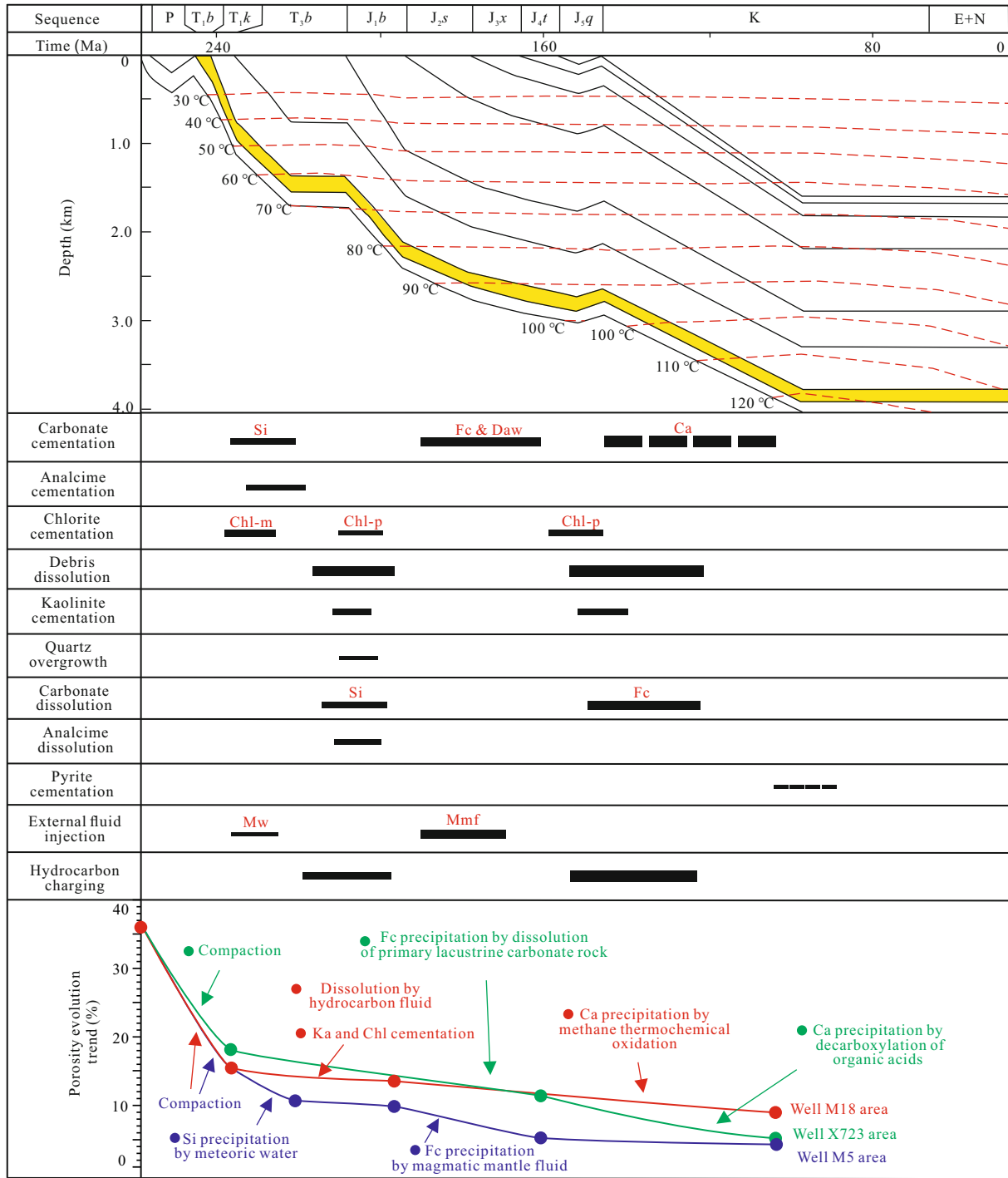
Figure 14. Diagenetic sequence and evolution of the reservoir properties in the T_1b. The primary porosities were obtained from the normal compaction curve using the method described by Wang et al. (2013). The dashed line shows that the deadlines of Mn-rich calcite and pyrite cementations are unclear. Si. Siderite; Fc. Ferroan calcite; Daw. dawsonite; Ca. Mn-rich calcite; Chl-m. chlorite membrane; Chl-p. pore-filling chlorite; Mw. meteoric water; Mmf. magmatic mantle fluid.

and debris were dissolved by deep fluid injection (with a range of 0.1%–5.2% and an average of 2.63%), and then the ferroan calcite was precipitated during the Early Jurassic. The content of ferroan calcite ranged from 2.5% to 10.08%, with an average of 4.67% (Fig. 14). Now the porosity of the reservoir is 1.17%–9.17%, with an average of 4.38%. Before the second hydrocarbon-charging, the reservoir has reached the degree of compactness. The oil and gas mainly relied on overpressure charging. The exploration potential of the reservoir is limited.

According to the results of the oil test, the reservoirs in the Well M5 area are characterized by poor oiliness, most of which are water layers or dry layers.

The reservoirs in the Well M18 area were affected by CO_2 fluid formed by methane thermochemical oxidation. Only Type I Mn-rich calcite was observed. After the first hydrocarbon-charging, the feldspar, debris and tuff matrix were dissolved (with a range of 1.1%–10.6% and an average of 5.43%) and then precipitated into kaolinite quartz overgrowth. The kaolinite

content was in the range of 0.4%–2.8% (average is 1.16%), and the quartz content was in the range of 0–1% (average is 0.4%). When the second hydrocarbon-charging occurred, a high amount of methane-containing fluid was injected and oxidized, which produced the precipitation of Type I Mn-rich calcite (with a range of 0.8%–5.6% and an average of 3.34%). The porosity of the reservoir is 4.1%–13.7% (average is 8.92%). Thus, the influence of Type I Mn-rich calcite cementation is limited. Under the improvement of dissolution, the quality of the reservoir is much higher. According to the results of the oil test, the oil production could be as high as 33.23 t·d⁻¹.

The reservoirs in the Well X723 area were affected by hydrocarbon source CO_2 fluids formed by decarboxylation of organic acids. A high amount of Type II Mn-rich calcite and minor ferroan calcite were observed. Prior to the second hydrocarbon-charging, the precipitation of ferroan calcite reduced the thin section porosity by 0.9%–3.8%, with an average of 1.47%. During the Late Jurassic to Early Cretaceous, the Type II Mn-rich calcite was formed with the second hydrocarbon charging, which caused the porosity of the reservoir to decrease by 1.43%–16.8%, with an average of 6.38% (Fig. 14). Although the porosity of the reservoir is 3.5%–9.8% (average is 5.8%), the oiliness property of the reservoir is good according to the results of the oil test from the Xinjiang Oilfield. The results of the oil test show that the oil production is 1.44 to 4.36 t·d⁻¹. According to trend of porosity evolution, before the second-stage hydrocarbon charging, the reservoir, the reservoir is medium-low porosity reservoir. During the second-stage hydrocarbon accumulation, the reservoir was becoming tight for Type II Mn-rich calcite cementation. By comparison, the reservoir in Well M5 area had become tight for ferroan calcite cementation before the second-stage hydrocarbon-charging. The hydrocarbon mainly relied on overpressure charge. Thus, it is can be concluded that the reservoir in Well X723 area is of relatively optimal exploration potential.

5 CONCLUSIONS

The carbonate cements in the Baikouquan Formation glutenite reservoir are dominated by Mn-rich calcite and ferroan calcite with occasional siderite and dawsonite. The Mn-rich calcite can be divided into Type I Mn-rich calcite and Type II Mn-rich calcite according to the Mn content. Siderite was characterized by dark spherulite crystal sand formed during 231–220 Ma. The ferroan calcite was characterized by poikilotopic blocky crystals and dark orange luminescence and formed at the same time as dawsonite during 185–142 Ma. The Mn-rich calcite was characterized by scattered patchy crystals and light-yellow luminescence and formed during148–105 Ma.

The siderite with -0.07‰ to +0.25‰ δ¹³C values is related to meteoric water. From the distribution range of siderite, the influence of meteoric water on the reservoir of research area is limited. The δ¹³C values (-5.06‰ to -2.43‰ and-12.37‰) of ferroan calcite suggest that the CO_2 displays a mantle-magmatic origin with minor decarboxylation of organic acid origin. The occurrence of authentic dawsonite also demonstrates the magmatic activity. Type I Mn-rich calcite with extremely depleted δ¹³C values (-54.99‰ to -27.04‰) shows that the methane gas was oxidized by high valence metal ions and then fixed in the form of carbonate mineral. Type II Mn-rich calcite with δ¹³C

values (-21.46‰ to -1.68‰) is a result of the mixing of the decarboxylation of organic acid and inorganic CO_2 injections.

The CO_2 injection does not lead to a net increase in porosity, nor does it completely affect the oiliness of the reservoir due to carbonate cementation. The differences in the content and formation time of carbonate cements and the degree of dissolution are significant factors resulting in the physical properties of the reservoir. Before the second hydrocarbon-charging, the reservoir in the Well M5 area reached the degree of compactness due to the cementation of siderite and ferroan calcite, with limited exploration potential. The reservoir cemented by Type II Mn-rich calcite is becoming tight during the second hydrocarbon-charging, with medium exploration potential. In the Well M18 area, CO_2 injection not only leads to the precipitation of Type I Mn-rich calcite but also creates smaller amounts of pores to enhance the porosity, which makes the reservoir have optimal exploration potential.

REFERENCES CITED

Anderson, T. F., Arthur, M. A., 1983. Stable Isotopes of Oxygen and Carbon and Their Application to Sedimentologic and Paleoenvironmental Problems. In: Stable Isotopes in Sedimentary Geology. *SEPM Society for Sedimentary Geology*, 1–1: 1–151. https://doi.org/10.2110/scn.83.01.0000

Arnott, R. W. C., 2003. The Role of Fluid- and Sediment-Gravity Flow Processes during Deposition of Deltaic Conglomerates (Cardium Formation, Upper Cretaceous), West-Central Alberta. *Bulletin of Canadian Petroleum Geology*, 51(4): 426–436. https://doi.org/10.2113/51.4.426

Baker, J. C., Bai, G. P., Hamilton, P. J., et al. 1995. Continental-Scale Magmatic Carbon Dioxide Seepage Recorded by Dawsonite in the Bowen-Gunnedah-Sydney Basin System, Eastern Australia. *SEPM Journal of Sedimentary Research*, 65(3): 522–530. https://doi.org/10.1306/d4268117-2b26-11d7-8648000102c1865d

Bath, A. H., Milodowski, A. E., Spiro, B., 1987. Diagenesis of Carbonate Cements in Permo-Triassic Sandstones in the Wessex and East Yorkshire-Lincolnshire Basins, UK: A Stable Isotope Study. *Geological Society, London, Special Publications*, 36(1): 173–190. https://doi.org/10.1144/gsl.sp.1987.036.01.14

Cant, D. J., Ethier, V. G., 1984. Lithology-Dependent Diagenetic Control of Reservoir Properties of Conglomerates, Falher Member, Elmworth Field, Alberta. *AAPG Bulletin*, 68(8): 1044–1054. https://doi.org/10.1306/ad4616c9-16f7-11d7-8645000102c1865d

Cao, J., Hu, W. X., Yao, S. P., et al., 2007. Carbon, Oxygen and Strontium Isotope Composition of Calcite Veins in the Carboniferous to Permian Source Sequences of the Junggar Basin: Implications on Petroleum Fluid Migration. *Acta Sedimentologica Sinica*, 25(5): 722–729 (in Chinese with English Abstract)

Cao, J., Yao, S. P., Jin, Z. J., et al., 2006. Petroleum Migration and Mixing in the Northwestern Junggar Basin (NW China): Constraints from Oil-Bearing Fluid Inclusion Analyses. *Organic Geochemistry*, 37(7): 827–846

Carothers, W. W., Adami, L. H., Rosenbauer, R. J., 1988. Experimental Oxygen Isotope Fractionation between Siderite-Water and Phosphoric Acid Liberated CO_2-Siderite. *Geochimicaet Cosmochimica Acta*, 52(10): 2445–2450. https://doi.org/10.1016/0016-7037(88)90302-X

Chen, X., Lu, H. X., Shu, L. S., et al., 2002. Study on Tectonic Evolution of Junnar Basin. *Geological Journal of China Universities*, 8(3): 257–267 (in Chinese with English Abstract)

Chen, Y. B., Pan, J. G., Zhang, H., et al., 2015. Characteristics of Fault Evolution in Mahu Slope Area of Junggar Basin and Its Implications to the Reservoir in the Lower Triassic Baikouquan Formation. *Natural Gas Geoscience*, 26(S1): 11–24 (in Chinese with English Abstract)

Chi, G., Giles, P. S., Williamson, M. A., et al., 2003. Diagenetic History and Porosity Evolution of Upper Carboniferous Sandstones from the Spring Valley #1 Well, Maritimes Basin, Canada-Implications for Reservoir Development. *Journal of Geochemical Exploration*, 80(2/3): 171–191. https://doi.org/10.1016/S0375-6742(03)00190-0

Chowdhury, A. H., Noble, J. P. A., 1996. Origin, Distribution and Significance of Carbonate Cements in the Albert Formation Reservoir Sandstones, New Brunswick, Canada. *Marine and Petroleum Geology*, 13(7): 837–846. https://doi.org/10.1016/0264-8172(96)00002-5

Cui, Y. F., Jones, S. J., Saville, C., et al., 2017. The Role Played by Carbonate Cementation in Controlling Reservoir Quality of the Triassic Skagerrak Formation, Norway. *Marine and Petroleum Geology*, 85: 316–331. https://doi.org/10.1016/j. marpetgeo.2017.05.020

Dos Anjos, S. M., De Ros, L. F., De Souza, R. S., et al., 2000. Depositional and Diagenetic Controls on the Reservoir Quality of Lower Cretaceous Pendência Sandstones, Potiguar Rift Basin, Brazil. *AAPG Bulletin*, 84: 1719–1742. https://doi.org/10.1306/8626c375-173b-11d7-8645000102c1865d

Duan, W., Luo, C. F., Lou, Z. H., et al., 2017. Diagenetic Differences Caused by the Charging of Natural Gases with Various Compositions—A Case Study on the Lower Zhuhai Formation Clastic Reservoirs in the WC-A Sag, the Pearl River Mouth Basin. *Marine and Petroleum Geology*, 81: 149–168. https://doi.org/10.1016/j.marpetgeo.2017.01.004

Dutton, S. P., 2008. Calcite Cement in Permian Deep-Water Sandstones, Delaware Basin, West Texas: Origin, Distribution, and Effect on Reservoir Properties. *AAPG Bulletin*, 92(6): 765–787. https://doi.org/10. 1306/01280807107

Edwards, E. C., 1934. Pliocene Conglomerates of Los Angeles Basin and Their Paleogeographic Significance. *AAPG Bulletin*, 18(6): 786–812. https://doi.org/10.1306/3d932c42-16b1-11d7-8645000102c1865d

El-Khatri, F., El-Ghali, M. A. K., Mansurbeg, H., et al., 2015. Diagenetic Alterations and Reservoir Quality Evolution of Lower Cretaceous Fluvial Sandstones: Nubian Formation, Sirt Basin, North-Central Libya. *Journal of Petroleum Geology*, 38(2): 217–239. https://doi.org/10.1111/jpg. 12607

Folk, R. L., Andrews, P. B., Lewis, D. W., 1970. Detrital Sedimentary Rock Classification and Nomenclature for Use in New Zealand. *New Zealand Journal of Geology and Geophysics*, 13(4): 937–968. https://doi.org/10. 1080/00288306.1970.10418211

Fontana, S., Nader, F. H., Morad, S., et al., 2014. Fluid-Rock Interactions Associated with Regional Tectonics and Basin Evolution. *Sedimentology*, 61(3): 660–690. https://doi.org/10.1111/sed.12073

Friedman, I., O'Neil, J. R., 1977. Compilation of Stable Isotope Fractionation Factors of Geochemical Interest. *US Geological Survey Chimica Acta*, 41: 1431–1438

Gao, Y. Q., Liu, L., Qu, X. Y., 2005. Genesis of Dawsonite and Its Indication Significance of CO_2 Migration and Accumulation. *Advance in Earth Sciences*, 20(10): 1083–1088 (in Chinese with English Abstract)

Gieskes, J., Mahn, C., Day, S., et al., 2005. A Study of the Chemistry of Pore Fluids and Authigenic Carbonates in Methane Seep Environments: Kodiak Trench, Hydrate Ridge, Monterey Bay, and Eel River Basin. *Chemical Geology*, 220(3/4): 329–345. https://doi.org/10.1016/j.chemgeo.2005.04.002

Guo, J. X., Li, Q., Wang, W. W., et al., 2017. Diagenetic Sequence and Genetic Mechanism of Silurian Tight Sandstone Reservoirs in the Eastern Tarim Basin, Northwest China. *Journal of Earth Science*, 28(6): 1109–1125. https://doi.org/10.1007/s12583-016-0939-2

Guo, Z. J., Han, B. F., Zhang, Y. Y., et al., 2010. Mesozoic and Cenozoic Crust-Mantle Interaction in the Central Asian Orogenic Belt: A Comparative Study of Mantle-Derived Magmatic Rocks in Northern Xinjiang. *Acta Petrologica Sinica*, 26(2): 431–439 (in Chinese with English Abstract)

Hao, Z. G., Fei, H. C., Hao, Q. Q., et al., 2018. The World's Largest Conglomerate Type Oilfield has been Discovered in the Junggar Basin of China. *Acta Geologica Sinica*: *English Edition*, 92(1): 394–395. https://doi.org/10.1111/1755-6724.13513

Helu, P. C., Rodolfo, V. V., Rodolfo, B. P., 1977. Origin and Distribution of Tertiary Conglomerates, Veracruz Basin, Mexico. *AAPG Bulletin*, 61(2): 207–226. https://doi.org/10.1306/c1ea3c26-16c9-11d7-8645000102c1865d

Hu, W. X., 2016. Origin and Indicators of Deep-Seated Fluids in Sedimentary Basins. *Bulletin of Mineralogy*, *Petrology and Geochemistry*, 35(5): 817–826, 806 (in Chinese with English Abstract)

Hu, W. X., Kang, X., Cao, J., et al., 2018. Thermochemical Oxidation of Methane Induced by High-Valence Metal Oxides in a Sedimentary Basin. *Nature Communications*, 9(1): 5131. https://doi.org/10.1038/s41467-018-07267-x

Irwin, H., Curtis, C., Coleman, M., 1977. Isotopic Evidence for Source of Diagenetic Carbonates Formed during Burial of Organic-Rich Sediments. *Nature*, 269(5625): 209–213. https://doi.org/10.1038/269209a0

Javanbakht, M., Wanas, H. A., Jafarian, A., et al., 2018. Carbonate Diagenesis in the Barremian-Aptian Tirgan Formation (Kopet-Dagh Basin, NE Iran): Petrographic, Geochemical and Reservoir Quality Constraints. *Journal of African Earth Sciences*, 144: 122–135. https://doi.org/10.1016/j. jafrearsci.2018.04.016

Jin, J., Kang, X., Hu, W. X., et al., 2017. Diagenesis and Its Influence on Coarse Clastic Reservoirs in the Baikouquan Formation of Western Slope of the Mahu Depression, Junngar Basin. *Oil & Gas Geology*, 38(2): 323–333, 406 (in Chinese with English Abstract)

Kang, X., Hu, W. X., Cao, J., et al., 2018. Selective Dissolution of Alkali Feldspars and Its Effect on Lower Triassic Sandy Conglomerate Reservoirs in the Junggar Basin, Northwestern China. *Geological Journal*, 53(2): 475–499. https://doi.org/10.1002/gj.2905

Kong, X. X., Jiang, Z. X., Han, C., et al., 2017. Genesis and Implications of the Composition and Sedimentary Structure of Fine-Grained Carbonate Rocks in the Shulu Sag. *Journal of Earth Science*, 28(6): 1047–1063. https://doi.org/10.1007/s12583-016-0927-x

Lei, Z. Y., Lu, B., Wei, Y. J., et al., 2005. Tectonic Evolution and Development and Distribution of Fans on Northwestern Edge of Junggar Basin. *Oil & Gas Geology*, 26(1): 86–91 (in Chinese with English Abstract)

Li, M., Jin, A. M., Lou, Z. H., et al., 2012. Formation Fluid Characteristics and Hydrocarbon Migration and Accumulation in Junggar Basin. *Oil & Gas Geology*, 33(4): 607–615 (in Chinese with English Abstract)

Liu, C. L., 1998. Carbon and Oxygen Isotopic Compositions of Lacustrine Carbonates of the Shahejie Formation in the Dongying Depression and Their Paleolimnological Significance. *Acta Sedimentologica Sinica*, 16(3): 109–114 (in Chinese with English Abstract)

Liu, H., Jiang, Z. X., Zhang, R. F., et al., 2012. Genetic Types of Daxing Conglomerate Bodies and Their Controls on Hydrocarbons in the Langgu Sag, Bohai Bay Basin, East China. *Petroleum Exploration and*

Development, 39(5): 545–551 (in Chinese with English Abstract)

Mack, G. H., Cole, D. R., Giordano, T. H., et al., 1991. Paleoclimatic Controls on Stable Oxygen and Carbon Isotopes in Caliche of the Abo Formation (Permian), South-Central New Mexico, USA. *SEPM Journal of Sedimentary Research*, 61: 458–472. https://doi.org/10.1306/d426773a-2b26-11d7-8648000102c1865d

Mahmic, O., Dypvik, H., Hammer, E., 2018. Diagenetic Influence on Reservoir Quality Evolution, Examples from Triassic Conglomerates/Arenites in the Edvard Grieg Field, Norwegian North Sea. *Marine and Petroleum Geology*, 93: 247–271. https://doi.org/10.1016/j.marpetgeo.2018.03.006

McBride, E. F., Parea, G. C., 2001. Origin of Highly Elongate, Calcite-Cemented Concretions in Some Italian Coastal Beach and Dune Sands. *Journal of Sedimentary Research*, 71(1): 82–87. https://doi.org/10.1306/041900710082

Milliken, K. L., McBride, E. F., Cavazza, W., et al., 1998. Geochemical History of Calcite Precipitation in Tertiary Sandstones, Northern Apennines, Italy. In: Morad, S., ed., Carbonate Cementation in Sandstones. Blackwell Publishing Ltd., Oxford. 213–239. https://doi.org/10.1002/9781444304893.ch10

Moore, J., Adams, M., Allis, R., et al., 2005. Mineralogical and Geochemical Consequences of the Long-Term Presence of CO₂ in Natural Reservoirs: An Example from the Springerville-St. Johns Field, Arizona, and New Mexico, USA. *Chemical Geology*, 217(3/4): 365–385. https://doi.org/10.1016/j.chemgeo.2004.12.019

Morad, S., 1998. Carbonate Cementation in Sandstones: Distribution Patterns and Geochemical Evolution. In: Morad, S., ed., Carbonate Cementation in Sandstones. Blackwell Publishing Ltd., Oxford. 1–26. https://doi.org/10.1002/9781444304893.ch1

Morad, S., Al-Ramadan, K., Ketzer, J. M., et al., 2010. The Impact of Diagenesis on the Heterogeneity of Sandstone Reservoirs: A Review of the Role of Depositional Facies and Sequence Stratigraphy. *AAPG Bulletin*, 94(8): 1267–1309. https://doi.org/10.1306/04211009178

Mozley, P. S., 1989. Relation between Depositional Environment and the Elemental Composition of Early Diagenetic Siderite. *Geology*, 17(8): 704–706. https://doi.org/10.1130/0091-7613(1989)0170704:rbdeat>2.3.co;2

Naehr, T. H., Eichhubl, P., Orphan, V. J., et al., 2007. Authigenic Carbonate Formation at Hydrocarbon Seeps in Continental Margin Sediments: A Comparative Study. *Deep Sea Research Part II: Topical Studies in Oceanography*, 54(11/12/13): 1268–1291. https://doi.org/10.1016/j.dsr2.2007.04.010

NEA (National Energy Administration), 2018. Petroleum and Natural Gas Industry Standard of the People's Republic of China: SY/T 5435-2018, Method of Grains-Size Analysis of Clastic Rock. National Energy Administration, Beijing (in Chinese)

Nodwell, B. J., Hart, B. S., 2006. Deeply-Rooted Paleobathymetric Control on the Deposition of the Falher F Conglomerate Trend, Wapiti Field, Deep Basin, Alberta. *Bulletin of Canadian Petroleum Geology*, 54(1): 1–21. https://doi.org/10.2113/54.1.1

O'Sullivan, T. P., Kiloh, K. D., Starzer, M. R., et al., 1991. Conglomerate Identification and Mapping Leads to Development Success in a Mature Alaskan Field. In: International Arctic Technology Conference, May 29–31, 1991. Anchorage, Alaska. SPE-22163-MS. https://doi.org/10.2118/22163-ms

Pan, J. G., Hao, F., Tan, K. J., et al., 2007. Characteristics of Natural Gas and Rules of Hydrocarbon Accumulation in the Northwest Margin of Junggar Basin. *Journal of Oil and Gas Technology*, 29(2): 20–23, 147 (in Chinese with English Abstract)

Qi, W., Pan, J. G., Wang, G. D., et al., 2015. Fluid Inclusion and Hydrocarbon Charge History for the Reservoir of Baikouquan Formation in the Mahu Sag, Junggar Basin. *Natural Gas Geoscience*, 26(S1): 64–71 (in Chinese with English Abstract)

Qiu, L. W., Yang, S. C., Qu, C. S., et al., 2017. A Comprehensive Porosity Prediction Model for the Upper Paleozoic Tight Sandstone Reservoir in the Daniudi Gas Field, Ordos Basin. *Journal of Earth Science*, 28(6): 1086–1096. https://doi.org/10.1007/s12583-016-0935-2

Qu, J. H., Zhang, L., Wu, J., et al., 2017. Characteristics of Sandy Conglomerate Reservoirs and Controlling Factors on Physical Properties of Baikouquan Formation in the Western Slope of Mahu Sag, Junggar Basin. *Xinjiang Petroleum Geology*, 38(1): 1–6 (in Chinese with English Abstract)

Roberts, H. H., Aharon, P., 1994. Hydrocarbon-Derived Carbonate Buildups of the Northern Gulf of Mexico Continental Slope: A Review of Submersible Investigations. *Geo-Marine Letters*, 14(2/3): 135–148. https://doi.org/10.1007/bf01203725

Rogers, J. P., 2007. New Reservoir Model from an Old Oil Field: Garfield Conglomerate Pool, Pawnee County, Kansas. *AAPG Bulletin*, 91(10): 1349–1365. https://doi.org/10.1306/06140706082

Rosenbaum, J., Sheppard, S. M. F., 1986. An Isotopic Study of Siderites, Dolomites and Ankerites at High Temperatures. *Geochimicaet Cosmochimica Acta*, 50(6): 1147–1150. https://doi.org/10.1016/0016-7037(86)90396-0

Rossi, C., Marfil, R., Ramseyer, K., et al., 2001. Facies-Related Diagenesis and Multiphase Siderite Cementation and Dissolution in the Reservoir Sandstones of the Khatatba Formation, Egypt's Western Desert. *SEPM Journal of Sedimentary Research*, 71(3): 459–472. https://doi.org/10.1306/2dc40955-0e47-11d7-8643000102c1865d

Sackett, W. M., Chung, H. M., 1979. Experimental Confirmation of the Lack of Carbon Isotope Exchange between Methane and Carbon Oxides at High Temperatures. *Geochimica et Cosmochimica Acta*, 43(2): 273–276. https://doi.org/10.1016/0016-7037(79)90246-1

Sensula, B., Boettger, T., Pazdur, A., et al., 2006. Carbon and Oxygen Isotope Composition of Organic Matter and Carbonates in Recent Lacustrine Sediments. *Geochronometria*, 25: 77–94. https://doi.org/10.1016/j.geobios.2004.10.004

Shelby, J. M., 1980. Geologic and Economic Significance of the Upper Morrow Chert Conglomerate Reservoir of the Anadarko Basin. *Journal of Petroleum Technology*, 32(3): 489–495. https://doi.org/10.2118/7837-pa

Stroker, T. M., Harris, N. B., Elliott, W. C., et al., 2013. Diagenesis of a Tight Gas Sand Reservoir: Upper Cretaceous Mesaverde Group, Piceance Basin, Colorado. *Marine and Petroleum Geology*, 40: 48–68. https://doi.org/10.1016/j.marpetgeo.2012.08.003

Suess, E., Whiticar, M. J., 1989. Methane-Derived CO₂ in Pore Fluids Expelled from the Oregon Subduction Zone. *Palaeogeography, Palaeoclimatology, Palaeoecology*, 71(1/2): 119–136. https://doi.org/10.1016/0031-0182(89)90033-3

Tan, K. J., Zhang, F., Wu, X. Z., et al., 2008. Basin-Range Coupling and Hydrocarbon Accumulation at the Northwestern Margin of the Junggar Basin. *Natural Gas Industry*, 28(5): 10–13, 136 (in Chinese with English Abstract)

Wang, J., Cao, Y. C., Liu, K. Y., et al., 2016. Pore Fluid Evolution, Distribution and Water-Rock Interactions of Carbonate Cements in Red-Bed Sandstone Reservoirs in the Dongying Depression, China. *Marine and Petroleum Geology*, 72: 279–294. https://doi.org/10.1016/j.marpetgeo.2016.02.018

Wang, K. Y., Li, J. F., Wan, D. D., et al., 2015. The Fluid Inclusion Evidence for the Charging Sequence of CO₂ and CH₄ in the Natural Gases Reservoir in Deeper Level Parts of Changling Depression. *Acta Petrologica Sinica*, 31(4): 1101–1107 (in Chinese with English Abstract)

Wang, Q., Zhuo, X. Z., Chen, G. J., et al., 2007. Characteristics of Carbon and Oxygen Isotopic Compositions of Carbonate Cements in Triassic

Yanchang Sandstone in Ordos Basin. *Natural Gas Industry*, 27(10): 28–32, 132–133 (in Chinese with English Abstract)

Wang, Y. Z., Cao, Y. C., Xi, K. L., et al., 2013. A Recovery Method for Porosity Evolution of Clastic Reservoirs with Geological Time: A Case Study from the Upper Submember of Es^4 in the Dongying Depression, Jiyang Subbasin. *Acta Petrolei Sinica*, 34(6): 1100–1111 (in Chinese with English Abstract)

Wang, Y. Z., Lin, M. R., Xi, K. L., et al., 2018. Characteristics and Origin of the Major Authigenic Minerals and Their Impacts on Reservoir Quality in the Permian Wutonggou Formation of Fukang Sag, Junggar Basin, Western China. *Marine and Petroleum Geology*, 97: 241–259. https://doi.org/10.1016/j.marpetgeo.2018.07.008

Whiticar, M. J., 1999. Carbon and Hydrogen Isotope Systematics of Bacterial Formation and Oxidation of Methane. *Chemical Geology*, 161(1/2/3): 291–314. https://doi.org/10.1016/s0009-2541(99)00092-3

Worden, R. H., 2006. Dawsonite Cement in the Triassic Lam Formation, Shabwa Basin, Yemen: A Natural Analogue for a Potential Mineral Product of Subsurface CO_2 Storage for Greenhouse Gas Reduction. *Marine and Petroleum Geology*, 23(1): 61–77. https://doi.org/10.1016/j.marpetgeo.2005.07.001

Xi, K. L., Cao, Y. C., Zhu, R. K., et al., 2016. Evidences of Localized CO_2-Induced Diagenesisin the Cretaceous Quantou Formation, Southern Songliao Basin, China. *International Journal of Greenhouse Gas Control*, 52(C): 155–174. https://doi.org/10.1016/j.ijggc.2016.07.010

Xiao, M., Yuan, X. J., Cheng, D. W., et al., 2018. Feldspar Dissolution and Its Influence on Reservoirs: A Case Study of the Lower Triassic Baikouquan Formation in the Northwest Margin of the Junggar Basin, China. *Geofluids*, 2018: 1–19. https://doi.org/10.1155/2018/6536419

Xu, G. S., Xu, Z. X., Gong, D. Y., et al., 2014. Relationship between Tanlu Fault and Hydrocarbon Accumulation in Liaozhong Sag, Bohai Bay, Eastern China. *Journal of Earth Science*, 25(2): 324–336. https://doi.org/10.1007/s12583-014-0432-8

Xu, X., Chen, C., Ding, T. F., et al., 2008. Discovery of Lisa Basalt Northwestern Edge of Junggar Basin and Its Geological Significance. *Xinjiang Geology*, 26(1): 9–16 (in Chinese with English Abstract)

Yang, T., Cao, Y. C., Friis, H., et al., 2018. Genesis and Distribution Pattern of Carbonate Cements in Lacustrine Deep-Water Gravity-Flow Sandstone Reservoirs in the Third Member of the Shahejie Formation in the Dongying Sag, Jiyang Depression, Eastern China. *Marine and Petroleum Geology*, 92: 547–564. https://doi.org/10.1016/j.marpetgeo.2017.11.020

Yuan, X. J., Qiao, H. S., 2002. Exploration of Subtle Reservoir in Prolific Depression of Bohai Bay Basin. *Oil & Gas Geology*, 23(2): 130–133 (in Chinese with English Abstract)

Zhu, N., Cao, Y. C., Xi, K. L., et al., 2019. DiagenesisAndphysical Properties Evolution of Sandy Conglomerate Reservoirs: A Case Study of Triassic Baikouquan Formation in Northern Slope Zone of Mahu Despression. *Journal of China University of Mining & Technology*, 48(5): 1102–1118. https://doi.org/10.13247/j.cnki.jcumt.001019 (in Chinese with English Abstract)

Zhu, S. F., Zhu, X. M., Wang, X. L., et al., 2012. Zeolite Diagenesis and Its Control on Petroleum Reservoir Quality of Permian in Northwestern Margin of Junggar Basin, China. *Science in China Series D*: *Earth Sciences*, 55(3): 386–396 (in Chinese with English Abstract)

Zou, H. Y., Hao, F., Zhang, B. Q., et al., 2005. Fluid-Conduit Framework and Its Control on Petroleum Accumulation in the Junggar Basin. *Earth Science*, 30(5): 609–616 (in Chinese with English Abstract)